

1 The evolution of the footwall to the Ronda subcontinental  
2 mantle peridotites: insights from the Nieves Unit (western  
3 Betic Cordillera)

4  
5 S. MAZZOLI<sup>1\*</sup>, A. MARTÍN-ALGARRA<sup>2</sup>, S. M. REDDY<sup>3</sup>, V. LÓPEZ SÁNCHEZ-  
6 VIZCAÍNO<sup>4</sup>, L. FEDELE<sup>1</sup> & A. NOVIELLO<sup>1</sup>

7  
8 <sup>1</sup>*Dipartimento Scienze della Terra, Università di Napoli Federico II, Largo San  
9 Marcellino 10, 80138 Naples, Italy*

10 <sup>2</sup>*Departamento de Estratigrafía y Paleontología, Universidad de Granada, 18071  
11 Granada, Spain*

12 <sup>3</sup>*The Institute for Geoscience Research & ARC COE for Core to Crust Fluid Systems,  
13 Department of Applied Geology, Curtin University of Technology, GPO Box U1987,  
14 Perth WA 6845, Australia*

15 <sup>4</sup>*Departamento de Geología (Unidad Asociada al IACT-CSIC, Granada), Escuela  
16 Politécnica Superior de Linares, Universidad de Jaén, 23700 Linares, Spain*

17  
18 \*Corresponding author (e-mail: stefano.mazzoli@unina.it)

19  
20 79778 characters of text (including spaces), 70 references, and 10 figures

21  
22 Abbreviated title: *Evolution of carbonates in the footwall of the Ronda peridotites*

23  
24 **Abstract:** Strongly heterogeneous deformation and extreme metamorphic gradients  
25 characterize the dominantly carbonate Nieves Unit in the footwall to the Ronda mantle  
26 extrusion wedge in the western Betic Cordillera. A well-developed foliation and mineral  
27 lineation, together with isoclinal intrafolial folds, occur in silicate-bearing,  
28 calcite/dolomite marbles within a *c.* 1,5 km-thick metamorphic aureole underlying the  
29 peridotites. For the inferred maximum pressure of 300 MPa, petrological investigations  
30 allow to define temperature ranges for the main zones of the metamorphic aureole:  
31 forsterite zone (> 510 °C; probably *c.* 700 °C), diopside zone (510–430 °C), tremolite  
32 zone (430–360 °C), and phlogopite zone (360–330 °C). Field structural analysis  
33 integrated with petrological, microstructural and EBSD textural data document large  
34 finite strains consistent with general shear within the metamorphic aureole, associated  
35 with NW-ward thrusting of the peridotites. On the other hand, post-kinematic silicate  
36 growth suggests that heat diffusion from the high-temperature peridotites continued  
37 after the final emplacement of the Ronda mantle extrusion wedge, leading to final  
38 zoning of the metamorphic aureole and to local partial annealing of calcite marble

39 textures, particularly in the highest-temperature zone of the thermally softened footwall  
40 carbonates. Following substantial cooling, renewed crustal shortening affected the  
41 whole Nieves Unit, resulting in widespread development of NE-trending meso-scale  
42 folds.

43  
44  
45

46 In the western Betic Cordillera (Fig. 1), high-temperature tectonic emplacement of the  
47 Ronda mantle peridotites (Fig. 2) on top of crustal units (e.g. Lundeen, 1978) is marked  
48 by the occurrence of a ‘metamorphic sole’ in the footwall rocks (e.g. Tubía *et al.*, 1997).  
49 In the southeastern, inner peridotite massif (Sierra Alpujata), a high pressure-  
50 temperature (P-T) shear zone records orogen-parallel (Tubía & Cuevas, 1986; Orozco  
51 and Alonso-Chaves, 2012), sinistral shear between the peridotites and the Alpine  
52 eclogites of the Ojen Unit. In contrast, in the outer peridotite massif of Sierra Bermeja  
53 located to the NW (Fig. 2), a high-T dynamothermal metamorphic aureole records  
54 orogen-perpendicular, foreland-ward thrusting of the peridotites on top of both low-P  
55 metamorphic rocks of the Guadaiza Unit (Cuevas *et al.*, 2006; Esteban *et al.*, 2008) and  
56 sedimentary successions of the Nieves Unit (Mazzoli & Martín-Algarra, 2011). These  
57 features have been interpreted in terms of deformation partitioning associated with  
58 oblique convergence during continental subduction and subsequent exhumation  
59 involving the coeval activity of kinematically linked systems of reverse, strike-slip and  
60 ‘normal-sense’ shear zones (Mazzoli & Martín-Algarra, 2011). In this context, orogen-  
61 parallel wrenching would have dominated the deeper, high-pressure portions of the  
62 continental subduction system, whereas orogen-perpendicular thrusting would have  
63 characterized the shallower, outer parts. Top-to-the-hinterland shear along the contact  
64 between the Ronda peridotites and overlying crustal rocks is consistent with extrusion of  
65 subcontinental mantle rocks of the overriding plate of the continental subduction system.  
66 Rapid exhumation of this extruding mantle wedge would have been further aided by  
67 strike-parallel extension and thinning of the crustal rocks overlying the peridotites (e.g.  
68 Tubía, 1994; Balanya *et al.*, 1997; Argles *et al.*, 1999; Platt *et al.*, 2003).

69 The crustal units lying in the footwall to the northwestern (i.e. outer) peridotite massif of  
70 Sierra Bermeja (Fig. 2) provide a unique opportunity to analyse strongly heterogeneous  
71 deformation associated with the ‘hot’ emplacement of a mantle wedge at shallow crustal  
72 levels. In the interior of the ultramafic massif, the contact at the base of the Ronda

73 peridotites is exposed in the Guadaiza River tectonic window (Fig. 2). There, the contact  
74 is marked by a dynamothermal metamorphic aureole formed at the expense of footwall  
75 rocks (Cuevas *et al.*, 2006; Esteban *et al.*, 2008). High-T metamorphism is well  
76 constrained by U/Pb SHRIMP dating of zircons from thin, syn-kinematic leucogranite  
77 sheets that emanated from the aureole and intruded the overlying peridotites, which  
78 provided ages of  $18.8 \pm 4.9$  Ma (Sánchez-Rodríguez & Gebauer, 2000) and  $21.8 \pm 0.5$   
79 Ma (Esteban *et al.*, 2007). The heat required for partial melting of footwall crustal rocks  
80 was provided by the fast emplacement of a *c.* 7 km thick, hot peridotite slab on top of the  
81 Guadaiza Unit, within the general framework of NW-directed overthrusting. This  
82 metamorphic aureole represents a low-viscosity, high-T ( $> 650$  °C) shear zone  
83 characterized by a marked strain gradient towards the contact with the overlying  
84 ultramafic rocks (Esteban *et al.*, 2008). On the other hand, the structure of footwall  
85 carbonate units occurring to the NW of the present leading edge of the Ronda mantle  
86 extrusion wedge has received much less consideration. The Nieves Unit rocks exposed  
87 in this area are characterized by a strong inverse metamorphic gradient (Martín-Algarra,  
88 1987; Mazzoli & Martín-Algarra, 2011). Within a *c.* 1.5 km thick zone, non-  
89 metamorphic limestones/dolostones pass to high-grade marbles in contact with the  
90 overlying peridotites. The metamorphic gradient is marked by silicate minerals  
91 occurring in the marbles, defining a series of zones varying in thickness from tens to  
92 several hundred metres and characterized by the occurrence of (moving towards the  
93 peridotites; Figs. 3 and 4): (i) talc, (ii) phlogopite, (iii) tremolite, (iv) diopside, and (v)  
94 forsterite. Extreme deformation gradients and changes in structural styles accompany the  
95 metamorphic gradient and are the focus of this study, along with the texture of silicate-  
96 bearing calcite marbles. Our results provide new insights into the metamorphic and  
97 deformation processes taking place in carbonate units adjacent to the Ronda high-T  
98 mantle wedge emplaced within the Betic orogen. In this (Behrmann, 1983) as well as in  
99 similar carbonate-rich orogenic belts such as the Alps (Pfiffner, 1982; Heitzmann, 1987;  
100 Burkhard, 1993) or the Apennines (Iannace *et al.*, 2005, 2007; Vitale & Mazzoli, 2005,  
101 2009), marbles may record important deformation processes in the upper crust. Although  
102 naturally and experimentally deformed carbonates have been the subject of intense  
103 laboratory investigations aimed at a better understanding of the localization of  
104 plastic/superplastic flow in these rocks (e.g. Schmid *et al.*, 1977, 1980, 1987; Rutter *et al.*,  
105 1994; Busch & Van der Pluijm, 1995; Badertscher & Burkhard, 2000; Bestmann *et al.*,  
106 2000; Pieri *et al.*, 2001a, 2001b; Badertscher *et al.*, 2002; Renner *et al.*, 2002; Ulrich

107 *et al.*, 2002; Barnhoorn *et al.*, 2004, 2005; Ebert *et al.* 2007a, b; Vitale *et al.*, 2007), the  
108 peculiar tectonic setting of the Nieves Unit allowed us analysing in detail the variation of  
109 mesoscopic and microscopic structural features and of textural fabrics of impure  
110 calcite/dolomite marbles for a range of temperature regimes – spanning over several  
111 hundreds of degrees Celsius – within the km-thick dynamothermal metamorphic aureole  
112 in the footwall to the Ronda peridotite mantle extrusion wedge.

113

## 114 **Geological Setting**

115

116 The Betic Cordillera, representing the westernmost part of the Alpine orogen in the  
117 Mediterranean region, resulted from the convergence between the African and Iberian  
118 plates since Late Cretaceous times (Andrieux *et al.*, 1970; Durand-Delga & Fontboté,  
119 1980; Martín Algarra & Vera, 2004). The Betic Cordillera, similarly to further Alpine  
120 mountain belts in the Mediterranean area, is traditionally subdivided into Internal (i.e.  
121 inner) and External (i.e. outer) Domains, with the Flysch Domain representing the  
122 suture between the two (Fig. 1). The area of the present study forms part of the Internal  
123 Domain of the western Betic Cordillera (Fig. 2). This domain is characterized by the  
124 occurrence of low-angle extensional shear zones of regional extent, reworking the pre-  
125 existing nappe structure (Balanya *et al.*, 1993; Argles *et al.*, 1999). These extensional  
126 contacts bound major allochthonous units characterized by varying tectonic and  
127 metamorphic pre-Alpine and Alpine evolutions (Sánchez-Navas *et al.*, 2012, and  
128 references therein). The lower allochthon (Alpujarride Complex) records variable  
129 Alpine P-T-t paths, generally characterized by high-pressure metamorphism followed  
130 by decompression and final cooling at 18–16 Ma (Sánchez Rodríguez & Gebauer, 2000).  
131 The upper allochthon (Malaguide Complex) generally lacks Alpine metamorphism  
132 (Martín-Algarra *et al.*, 2009). A general lack of Alpine metamorphism characterizes  
133 also the so-called ‘Frontal Units’ of the Internal Domain, one of which – i.e. the Nieves  
134 Unit – is the subject of the present study; these units are thrust over the Flysch and  
135 External Domains (Fig. 2). A series of unconformable marine basin successions  
136 (Viñuela Group; Martín-Algarra, 1987) sit on top of the collapsed nappe pile.  
137 Deposition of these Burdigalian clastic sediments predated backthrusting of the Flysch  
138 Domain units above the Internal Domain (Fig. 2).

139 The Ronda peridotites form the lower portion of the traditionally recognized highest  
140 Alpujarride nappe in the area. Above the mantle rocks, the highly attenuated Jubrique

141 crustal section – including granulitic gneisses, migmatites, high-to-low grade pre-  
142 Mesozoic metapelites, and Triassic metasediments at the top – is characterized by  
143 isograds lying roughly parallel to the lithological contacts and to the regional foliation  
144 (Balanyà *et al.*, 1993, 1997; Tubía, 1994; Tubía *et al.*, 1997). Although the Ronda  
145 peridotites and the Jubrique crustal section are traditionally grouped into the so-called  
146 Los Reales Nappe (Didon *et al.*, 1973; Fig. 2), the contact between mantle and crustal  
147 rocks consists of a high-T ( $T = 780\text{ °C}$ ) major shear zone responsible for partial  
148 exhumation of the peridotites (van Wees *et al.*, 1992; Balanyà *et al.*, 1993; Van der Wal  
149 & Vissers, 1996; Argles *et al.*, 1999) and representing the top of the mantle extrusion  
150 wedge according to Mazzoli & Martín-Algarra (2011). The Ronda peridotites are  
151 mainly composed of plagioclase and spinel lherzolites (with subordinate garnet  
152 lherzolites towards the top of the ultramafic body), mafic layers, and minor dunites and  
153 harzburgites (Obata, 1980; Van der Wal & Vissers, 1996; Garrido *et al.*, 2011). They  
154 form a series of massifs, the larger being those of Sierras Alpujata and Bermeja, where  
155 ultramafic rocks are tectonically emplaced onto ‘Blanca-type’ Alpujarride units or onto  
156 ‘Frontal Units’ of the Internal Domain (Nieves Unit; Martín-Algarra, 1987; Fig. 2).  
157 The ‘Blanca-type’ units (Ojen, Guadaiza, and Yunquera) share a typical Alpujarride  
158 succession, with high-grade metapelites at the bottom, whose protoliths are of a  
159 presumed Palaeozoic and Triassic age, and HT-marbles at the top, of probable Triassic,  
160 and perhaps younger, sedimentary age (Hoeppener *et al.*, 1963, 1964). Stratigraphic  
161 data (Martín-Algarra & Estévez, 1984; Martín-Algarra, 1987) and zircon geochronology  
162 (Esteban *et al.*, 2011) demonstrate the Early Miocene age (c. 20–22 Ma) of the high-T  
163 Alpine metamorphism that affects all ‘Blanca-type’ units, which was related to their  
164 tectonic emplacement below the Ronda peridotites. However, the Ojen Unit records a  
165 first stage of high-P metamorphic conditions ( $T = 790\text{ °C}$ ,  $P \geq 1.7\text{ GPa}$ ; Tubía & Gil-  
166 Iburguchi, 1991) with a temperature peak dated at  $19.9 \pm 1.7\text{ Ma}$  (Sánchez-Rodríguez &  
167 Gebauer, 2000) in eclogites derived from former Jurassic metabasites dated at  $183 \pm 3$   
168 Ma. Fast exhumation (at a rate of  $6\text{ km Ma}^{-1}$ ; Orozco and Alonso-Chaves, 2012, and  
169 references therein) of these high-P rocks, rather than by ultra-rapid extension and  
170 extreme thinning of an unrealistic ( $> 50\text{ km}$  thick) nappe stack, is likely to have  
171 occurred within a subduction channel (Mazzoli and Martín-Algarra, 2011). On the  
172 contrary, the Guadaiza Unit displays exclusively evidence of low-P metamorphic  
173 conditions ( $T = 675\text{–}750\text{ °C}$ ,  $P = 550\text{–}650\text{ MPa}$ ; Esteban *et al.*, 2008). Finally, the  
174 Yunquera Unit consists of an extremely thin, discontinuously exposed tectonic slice that

175 was possibly produced by tectonic delamination of the Ojen Unit in the footwall to the  
176 Ronda peridotite wedge, as it also preserves relics of high-P metamorphism (Martín-  
177 Algarra, 1987). In the area of the present study, the Yunquera Unit is locally exposed in  
178 the footwall to the Ronda peridotites (Fig. 3). Both of these units record NW-directed  
179 thrusting over the Nieves Unit (Esteban *et al.*, 2005; Mazzoli & Martín-Algarra, 2011).

180

### 181 **The Nieves Unit**

182

183 The Nieves Unit (Dürr, 1967) is formed by a non-metamorphic – apart from the aureole  
184 at the contact with the Ronda peridotites – Triassic to Lower Miocene sedimentary  
185 succession (Fig. 4). A few tens of metres thick sole of strongly sheared, brown scaly  
186 clays of the Campo de Gibraltar Complex, including frequent quatzarenites and rare  
187 micaceous sandstone phacoids, commonly occurs in its immediate footwall. This sole  
188 constitutes a strongly thinned and stretched tectonic *mélange* interposed between the  
189 Nieves Unit and the tectonically underlying Penibetic Units of the External Domain.  
190 The hanging wall to the Nieves Unit is constituted by the Los Reales Nappe  
191 (Alpujarride Complex), which in turn is overlain by the Malaguide Complex. Both  
192 complexes thin rapidly northwards, forming a wedge-shaped, broad antiformal structure  
193 whose core is occupied by the folded succession of the Nieves Unit (Fig. 4). The Ronda  
194 peridotites at the base of the so-called Los Reales Nappe represent the thickest part of  
195 the wedge but rapidly disappear towards the N due to the hanging-wall cutoff above the  
196 Nieves Unit (Fig. 4). The Jubrique crustal succession overlying the peridotites is mostly  
197 eroded above the main outcrop of the Nieves Unit; however, thin remnants are  
198 preserved as small klippen on top of the youngest beds of the Nieves succession (Nava  
199 Breccia Fm., see below), being in turn locally overlain by klippen of Malaguide  
200 Palaeozoic rocks (Fig. 3).

201

### 202 *Stratigraphy*

203

204 The stratigraphic succession of the Nieves Unit includes a *c.* 1.5 km thick Meso-  
205 Cenozoic succession (Fig. 4) mainly made of carbonate formations showing typical  
206 Alpine-Mediterranean facies.

207 The lowest formation is made of very thick- to medium-bedded Norian dolostones  
208 showing shallow marine facies and a cumulative thickness in excess of 1 km (unit 1 in

209 Fig. 4). Fine-grained terrigenous intercalations are locally present, especially in the  
210 lowest part and towards the upper third part of the succession.

211 The top of the Triassic succession is made of up to 200 m thick, basinal, greyish and  
212 locally yellowish marls alternating with hemipelagic micritic limestones (unit 2 in Fig. 4)  
213 that gradually pass upwards (and laterally northwards) to black to dark-grey limestones  
214 (unit 3 in Fig. 4). The Jurassic-Paleogene part of the succession (unit 4 in Fig. 4) starts  
215 with cherty limestones (usually less than 200 m thick), locally including carbonate  
216 turbidites rich in crinoidal bioclasts, mass-flow limestone breccias and red nodular  
217 limestone horizons bearing lower Hettangian and Sinemurian ammonites. The  
218 succession becomes marly towards the top of the Lower Jurassic section. Upwards, a  
219 condensed pelagic succession develops (Martín-Algarra *et al.*, 1998; O'Dogherty *et al.*,  
220 2001). It is made of Middle Jurassic red nodular and cherty limestones and radiolarian  
221 cherts, Upper Jurassic and lowermost Cretaceous marly and cherty limestones with  
222 ammonites, *Saccocoma*, *Aptychus* and *Calpionella* limestones (unit 5 in Fig. 4). The  
223 latter are followed by varicoloured marls bearing Paleogene to Aquitanian planktonic  
224 foraminifera and calcareous nannoplankton, with intercalated carbonate turbidites. The  
225 succession of the Nieves Unit is topped by a Lower Miocene, rauhwacke-like,  
226 continental carbonate breccia (Nava Breccia Fm; unit 6 in Fig. 4). This breccia is  
227 cartographically unconformable onto the older formations of the Nieves Unit, although  
228 being intensely folded together with the underlying part of the succession. The  
229 palaeogeographic and palaeotectonic significance of the Nava Breccia Fm –  
230 representing the youngest deposit involved in the deformation and, therefore, a key  
231 stratigraphic unit of the study area – has been investigated by Martín-Algarra & Estévez  
232 (1984) and Martín-Algarra (1987, 2004) to which the interested reader is referred to.

233 Towards the SE, the sedimentary succession described above is overthrust by the  
234 Ronda peridotites (Fig. 5A), intensely deformed and transformed into a metamorphic  
235 succession essentially made of both calcite and dolomite marbles, locally rich in quartz  
236 lenses and levels, with subordinate intercalations of calcschists, calcareous metapelites  
237 and paramphibolites (Figs. 5B-F and 6A-E). This transformation can be laterally  
238 followed in the field, bed by bed, from non-metamorphic lithotypes to high-grade rocks  
239 (see below), especially in the Torrecilla area (Fig. 2).

240

241 *Structure*

242

243 The map-scale structure of the Nieves Unit is dominated by a NW-verging, overturned  
244 syncline (Figs. 3 and 4) that can be traced for several tens of kilometres along strike  
245 (Fig. 2). Regional folding around a gently NE-plunging axis (Fig. 7A) is well defined  
246 also statistically by the distribution of the poles to bedding ( $S_0$ ) and to the main  
247 composite planar fabric ( $S_0$ - $S_1$ ) measured from the metamorphic aureole (see below).  
248 The stratigraphic succession, dominated by limestones and dolostones in the normal  
249 limb of the syncline, gives way to calcite/dolomite marbles in the overturned fold limb,  
250 which is characterized by the previously mentioned dramatic metamorphic gradient.  
251 Each stratigraphic unit mapped in the normal fold limb has a corresponding, well-  
252 defined high-T equivalent in the metamorphic aureole of the overturned limb (Fig 4).  
253 Here the original bedding, marked by clearly distinguishable lithological changes (Fig  
254 5B), is generally parallel to a foliation, defining a composite ( $S_0$ - $S_1$ ) planar fabric (Fig  
255 5C-E). A dominantly SE-plunging (Fig. 7B) mineral lineation ( $L_1$ ), defined by  
256 elongated calcite/dolomite and locally tremolite crystals (Fig. 6A), occurs on the  
257 composite ( $S_0$ - $S_1$ ) planar fabric. Isoclinal intrafolial folds (Fig. 6B) display variably  
258 plunging hinge lines (mainly tending to lie close to  $L_1$ ; Fig. 7C), and dominantly SSE  
259 dipping axial surfaces (Fig. 7D). Field evidence for non-coaxial strain is rare; where  
260 observed, it is represented by a sigmoidal foliation and S-C-C' structures indicating top-  
261 to-the-NW sense of shear.

262 Minor NE-SW trending, open to close parasitic folds are associated with the regional  
263 syncline in the non-metamorphic sedimentary succession of the Nieves Unit. They are  
264 asymmetric (*s*-shaped looking towards NE) in the normal limb of the regional syncline  
265 (Fig. 6D), and symmetric (*m*-shaped) in its core (hinge region). An axial plane cleavage  
266 – or weakly convergent cleavage in competent beds – is associated with these folds.  
267 This foliation is intensely developed in the core of the regional syncline, particularly in  
268 Jurassic-Paleogene units.

269 Open to tight, post-metamorphic folds deform the main composite planar fabric ( $S_0$ - $S_1$ )  
270 in the metamorphosed overturned limb of the regional syncline (Fig. 6C), as well as  
271 bedding ( $S_0$ ) in its core and in the normal fold limb. These folds show NE-SW trending  
272 hinge lines (Fig. 7E) and both SE- and NW-dipping axial surfaces (Fig. 7F). A variably  
273 developed second-phase cleavage ( $S_2$ ) is associated with these folds, being axial-planar  
274 to them in less competent lithologies and forming convergent cleavage fans in more  
275 competent beds. The lack of neo-formed metamorphic minerals on  $S_2$  cleavage surfaces  
276 suggests that this planar structure developed at very low-grade conditions. Within the



277 metamorphic aureole, the intersection between  $S_2$  and the composite planar fabric ( $S_0$ - $S_1$ )  
278 defines a dominantly NE-trending linear structure parallel to the late fold hinges. A  
279 similar NE-SW trend is also defined by calcite rods developed along buckled marble-  
280 phyllite interfaces in the metamorphic units (the phyllites representing metamorphosed  
281 terrigenous intercalations in the carbonates).  
282 The youngest shortening-related structures within the Nieves Unit include scattered  
283 kink bands (Fig. 6E), whereas high-angle, dominantly extensional faults dissect all of  
284 the previous structures as well as the main nappe contacts.

285

### 286 **Petrology and Microstructural Analysis: Materials and Methods**

287

288 In the following we describe the most representative mineral assemblages and textures  
289 of 25 selected silicate-bearing marbles sampled in the studied metamorphic aureole  
290 (Figs. 3 and 4). Rocks were sampled along the A-397 road (km 17 to 21), near the Cerro  
291 de los Cascajares peak, crossing the phlogopite, tremolite, diopside, and forsterite  
292 metamorphic zones defined by Martín-Algarra (1987), and in further outcrops, within  
293 the forsterite zone, close to the Cerro Alcojona peak (Table 1).

294 A first approximation to metamorphic conditions for the impure marbles of the Sierra de  
295 las Nieves contact aureole was reached by means of appropriate petrogenetic grids. P-T  
296 phase diagram projections (Fig. 9) were calculated using Perple X (Connolly, 1990,  
297 2009) for the mixed-volatile  $K_2O$ - $CaO$ - $MgO$ - $Al_2O_3$ - $SiO_2$ - $H_2O$ - $CO_2$  (KCMASHC)  
298 system, following the method by Connolly & Trommsdorff (1991). Thermodynamic  
299 mineral data and the equation of state for  $H_2O$ - $CO_2$  fluids were those of Holland &  
300 Powell (1998, revised version 2002). The only solution model considered in the  
301 calculations was that of the  $H_2O$ - $CO_2$  fluid (Trommsdorff & Connolly, 1991). In the  
302 figures and following text, F represents the fluid composition expressed as  $X_{CO_2}$  [=   
303  $CO_2/(CO_2+H_2O)$ ] and the numbers in parentheses are those of the pseudocompounds  
304 (Connolly & Kerrick, 1987) used by Perple X to represent fluid composition. All other  
305 phases were taken as pure phases and the following solid end-members were considered  
306 (abbreviations after Whitney & Evans, 2010): calcite (Cal), clinocllore (Clc),  
307 clinohumite (Chu), diopside (Di), dolomite (Dol), forsterite (Fo), microcline (Mc),  
308 phlogopite (Phl), quartz (Qz), tremolite (Tr), and spinel (Spl).

309 This was a realistic simplification because most of the phases observed in the rocks  
310 approach pure end-members compositions. In fact,  $X_{Mg}$  [=  $Mg/(Mg+Fe)$ ] in all

311 ferromagnesian phases (amphibole, chlorite, clinohumite, clinopyroxene, olivine, and  
312 spinel) commonly ranges between 0.90 and 0.95 (but in many cases it exceeds these  
313 values) in the impure marble samples. Likewise, both calcite and dolomite display  
314 compositions close to stoichiometry. Some exceptions are reported for phlogopite (with  
315 up to 1.6 atoms per formula unit – a.p.f.u. – of total Al; 11 oxygens), chlorite (with up  
316 to 2.6 a.p.f.u. of total Al; 14 oxygens) and clinohumite (very rich in fluorine: up to 1.7  
317 a.p.f.u.; 13 cations). Pargasitic amphibole and clinopyroxene ( $X_{Mg} \sim 0.60$ ) occurring in  
318 some pelitic intercalations also differ from the general trend, but these assemblages  
319 were not taken into account in the calculations. Uncertainties associated with ignoring  
320 these solid solutions are discussed below.

321 Electron backscatter diffraction (EBSD) data collected by scanning electron microscope  
322 (SEM) were used for textural analysis of seven calcite marble samples and one dolomite  
323 marble sample from the metamorphic aureole found in the overturned limb of the  
324 regional syncline affecting the Nieves Unit. Samples 09A-1 and 09A-3 are from the  
325 forsterite zone; sample 09A-7 is from the diopside zone; samples 09A-12, 09A-15, 09A-  
326 18 and 09A-19 are from the tremolite zone, and sample 09A-20 is from the phlogopite  
327 zone. Thin sections of each sample were cut parallel to the mineral lineation (X) and  
328 perpendicular to the composite planar fabric ( $S_0-S_1 = XY$ ; see below). Thin sections  
329 were mechanically polished using down to 1  $\mu\text{m}$  diamond paste. To remove  
330 mechanically-induced surface damage, a further 3 hours of polishing, with 0.06  $\mu\text{m}$   
331 colloidal silica, was undertaken. Thin sections were coated with a thin layer of carbon to  
332 prevent surface charging in the SEM. EBSD analysis was undertaken on a ZEISS-EVO  
333 40XVP scanning electron microscope at Curtin University, Perth, Western Australia.  
334 Collection, indexing and analysis of electron backscatter diffraction patterns (EBSP)  
335 were carried out using the CHANNEL 5.10 software by Oxford Instruments. The EBSD  
336 data were noise reduced using a ‘wildspike’ correction and a 7-neighbour zero solution  
337 extrapolation following standard procedures (Reddy *et al.*, 2007). Orientation data were  
338 plotted with respect to the mesoscopic sample lineation and foliation (X direction and  
339 XY plane respectively), as lower hemisphere, equal area projections, using CHANNEL  
340 Mambo software. Pole figure orientation data were plotted in terms of all of the  
341 collected EBSD data (‘all data’) and as one point per grain data. For the latter, grain  
342 boundaries were defined by misorientation boundaries in excess of  $10^\circ$ , and any twin  
343 boundaries identified by a  $78^\circ$  rotation around  $\langle 20-21 \rangle$  were ignored.  
344 Finally, thin section microphotographs (acquired using a Leica DFC280 digital camera

345 mounted on a Leitz Laborlux 12 Pol polarizing microscope) were employed for modal  
346 and carbonate grain size analyses of the same samples used for the textural analysis.  
347 Modal analyses were aimed to the quantification of the volume abundances of non-  
348 carbonate minerals (i.e. ‘impurities’, or secondary phases) and were performed using a  
349 point counting routine of the Leica QWinPlus V3.2.1 image analysis software.  
350 Carbonate grain size analyses were performed using the ImageJ 1.46r image analysis  
351 software (further details are summarized in Table 2).

352

### 353 **Petrology and Microstructural Analysis: Results**

354

#### 355 *Petrography of silicate-bearing marbles*

356

357 The studied rocks consist of impure marbles containing relatively low amounts (6.5% to  
358 17.8% for the samples listed in Table 2) of non-carbonate minerals. Most of lower-T  
359 dolomite marbles can be defined as phlogopite-tremolite marbles with the significant  
360 local occurrence of chlorite or spinel (Table 1). They display a granoblastic texture with  
361 a rough foliation defined by the preferred orientation of fine grained aggregates of  
362 phlogopite, which may be also strongly folded (Figs. 8A-B). Phlogopite is also found as  
363 randomly oriented, small, isolated flakes and as randomly oriented, hypidioblastic larger  
364 flakes, commonly related to other silicates such as spinel and tremolite (e.g. sample  
365 09A-11, Fig. 8D). Large, randomly oriented phlogopites may, however, display  
366 distinctive undulose extinction. Colourless *amphibole* is commonly associated with  
367 calcite grains or levels, and occurs as prismatic to acicular crystals rich in small  
368 dolomite inclusions. Amphibole grains are isolated (Fig. 8F) or give place to palmed  
369 aggregates, in many places with clear preferred orientation parallel to the main foliation  
370 (Fig. 8C). Chlorite (sample 09A-16; Table 1) appears as large hypidioblastic flakes  
371 having plenty of phlogopite and dolomite inclusions. Spinel (sample 09A-11; Table 1)  
372 is found as xeno- to hypidioblastic, isolated grains that grew after – or related to –  
373 recrystallized phlogopite flakes (Fig. 8D).

374 Moving towards the peridotites, clinopyroxene is found in modal quartz-rich rocks  
375 (with the exception of marble sample 09A-1; Table 1), usually consisting of pelitic or  
376 quartz-feldspar-bearing intercalations within the calcite marbles. Clinopyroxene appears  
377 as green pleochroic, isolated crystals or aggregates with largely variable grain size at the  
378 contact between quartz-rich and carbonate-rich levels (Fig. 8E). Highly birefringent

379 scapolite poikiloblasts as well as minor amounts of alkali-feldspar, phlogopite and  
380 tremolite (Fig. 8E) also appear in some of these rocks, (that will not be taken into  
381 account in the phase diagram calculations below).

382 Within a few tens of metres to the peridotite, olivine-bearing calcite or calcite-dolomite  
383 marbles contain variable silicate assemblages and textures (Table 1). The most  
384 representative assemblages consist of Cal + Dol + Phl + Amp + Ol  $\pm$  Chu  $\pm$  Spl  
385 (abbreviations after Whitney & Evans, 2010), while clinopyroxene and chlorite have  
386 been found only in one sample within this zone. Silicate minerals typically display  
387 textural characteristics indicative of static growth post-dating deformation (e.g. large  
388 grain size, lack of preferred orientation, hypidioblastic shape; Fig. 8F). In further  
389 instances silicates occur as non-deformed aggregates of mostly xenoblastic grains with  
390 complex interrelationships reflecting metamorphic reactions (Fig. 8G). This is also  
391 indicated by the occurrence of late poikiloblasts of dolomite surrounding these  
392 aggregates.

393 In tremolite and higher-T mineral zones, centimetre-scale phlogopite-tremolite clots that  
394 clearly displaced and overgrew the main composite planar fabric ( $S_0$ - $S_1$ ) are observed  
395 also in outcrop (Fig. 5F). However, as mentioned previously, tremolite crystals also  
396 occur on the main composite foliation.

397

### 398 *Metamorphic analysis*

399

400 A simplified petrogenetic grid for the KCMASHC system and a wide P-T range is  
401 shown in Fig. 9 (A). Both fluid-present and fluid-absent univariant equilibria occur. The  
402 most striking feature of this P-T projection is that most of the curves display very steep  
403 and remarkably constant Clapeyron slopes, thus defining narrow zones in which the  
404 stability of phase assemblages is strongly dependent on temperature and fluid  
405 composition (e.g. Fig. 9B). Calculations for the  $K_2O$ -CaO-FeO-MgO- $Al_2O_3$ - $SiO_2$ - $H_2O$ -  
406  $CO_2$  system (KCFMASHC) that take into account the limited Fe-Mg solid solution ( $X_{Mg}$   
407 usually  $< 0.95$ ) in the ferromagnesian minerals reveals a negligible shift towards higher  
408 temperatures of the reactions of interest (not shown in the figures) and will not be  
409 considered in the following. The effect of the solid solutions models for phlogopite  
410 (between the phlogopite-eastonite end-members) and chlorite (between the clinochlore-  
411 amesite end-members), applying for the Al amounts observed in these minerals, has  
412 also been tested. As a general trend, for the reactions of interest, pseudounivariant

413 curves with Al-richer pseudocompounds shift toward higher temperatures. However,  
414 within the range of the limited solid solutions observed in the studied minerals, this is a  
415 minor effect when compared with that of the changing fluid phase composition and will  
416 not be further considered. As a result, in the following analysis univariant reactions with  
417 steep Clapeyron slopes (especially those involving phlogopite or chlorite) should be  
418 regarded as indicators of the minimum temperature conditions at which observed  
419 minerals or assemblages were stable. In contrast with these steep reactions, only a few  
420 reactions display gentle or variable Clapeyron slopes. Among these, the reaction  $\text{Cal} +$   
421  $\text{Tr} + \text{Fo} = \text{H}_2\text{O} + \text{Di} + \text{Dol}$  sets the highest pressure limit for the observed mineral  
422 assemblage, in which calcite, amphibole and olivine coexist. Accordingly, all further P-  
423 T projections (Fig. 9B to D) correspond to the expanded field between 50 and 500 MPa,  
424 and between 300 and 700 °C for the same KCMASHC system. This pressure range is  
425 consistent with the previously described geological setting of the contact aureole. Based  
426 on geological evidence pointing to a burial depth of *c.* 10 km (including the mantle  
427 peridotites; Mazzoli & Martín-Algarra, 2011), maximum pressures may be further  
428 constrained to around 300 MPa. These P conditions are roughly similar to those  
429 suggested by Esteban et al. (2008) for the Guadaiza River tectonic window just south of  
430 our study area (Fig. 2).

431 Metamorphic conditions for the occurrence of phlogopite, amphibole, spinel and  
432 chlorite in the studied aureole can be discussed from selected representative equilibria  
433 shown in Fig. 9 (B) and summarized in Fig. 9 (D). Minimum temperature conditions for  
434 the first occurrence of phlogopite in the dolomite-bearing rocks are controlled by the  
435 univariant reaction indicating the breakdown of detrital microcline (e.g. Rice, 1977) in  
436 the presence of water-rich fluid:  $\text{F}(\text{H}_2\text{O}) + \text{Dol} + \text{Mc} = \text{F}(\text{CO}_{6.6}) + \text{Cal} + \text{Phl}$ .  
437 Depending on the latter parameter, the Phl-in reaction turns to be projected as  
438 pseudounivariant equilibria (Connolly & Trommsdorff, 1991), represented as grey thin  
439 dashed curves, in which only one (that of coexisting 6.6 and 9.9 pseudocompounds) is  
440 labelled with the complete reaction and all the remaining ones are labelled with the  
441 mean value of coexisting pseudocompounds (Fig. 9B). As a result, it can be deduced  
442 that the first appearance of phlogopite can take place in a wide divariant field with  
443 increasing temperature conditions for CO<sub>2</sub>-richer fluids. For the estimated maximum  
444 pressure of 300 MPa (thick grey dashed line in Fig. 9D), the minimum temperature for  
445 the stability of phlogopite is 350 °C.

446 A similar analysis can be carried out for defining the *tremolite*-in conditions. In  
 447 dolomite and quartz-bearing marbles, this takes place due to the univariant reaction:  
 448  $F(H_2O) + Qz + Dol = F(CO6.6) + Cal + Tr$ . The divariant field defined by  
 449 pseudounivariant equilibria (only that corresponding to pseudocompounds 16.4 and  
 450 19.7 is represented with a thin black dashed curve) is shaded in light grey in Fig. 9 (B).  
 451 In pure calcite marbles the univariant tremolite-in reaction is:  $F(H_2O) + Qz + Cal + Phl$   
 452  $= F(CO6.6) + Tr + Mc$ ; sample pseudounivariant equilibrium with pseudocompounds  
 453 13.1 and 16.4 is represented with a thin continuous black curve and the divariant field is  
 454 shaded in darker grey in Fig. 9 (B). Thus, at 300 MPa, the minimum temperature for the  
 455 appearance of tremolite ranges from 360 °C in quartz-bearing dolomite marbles to 410  
 456 °C in calcite marbles (Fig. 9D). In the studied selected samples the latter rock type is  
 457 more abundant than the former one (cf., Table 1).

458 The first appearance of *spinel* in the petrogenetic grids of Fig. 9 (B, D) is indicated by  
 459 the fluid-absent univariant reaction:  $Tr + Dol + Mc + Clc = Cal + Phl + Spl + Qz$  at an  
 460 almost constant temperature of 430 °C. At higher T (500 °C at 300 MPa), the reaction  
 461  $Dol + Mc + Clc = Cal + Phl + Spl + Qz + F$  takes place. Both are clinocllore  
 462 breakdown reactions yielding the same solid products. The coexistence of Cal, Phl and  
 463 Spl is well documented (e.g. Fig. 8D), whereas Qz is always lacking. This can be easily  
 464 explained taking into account that the chlorite end-member phase employed in the  
 465 calculations (clinocllore) is richer in Si than real chlorites observed in the rocks (3 Si  
 466 a.p.f.u. versus 2.5 Si a.p.f.u.). Irrespective of composition, *chlorite* is stable in the  
 467 KCMASHC system, at Al-rich compositions, in the whole considered P-T range.

468 Selected relevant equilibria explaining the occurrence of diopside, olivine, and  
 469 clinohumite are displayed in Fig. 9 (C). Observed *diopside*-bearing rocks are lacking in  
 470 dolomite and very rich in quartz (Table 1). The first appearance of diopside in calcite  
 471 marbles takes place through the univariant reaction:  $F(H_2O) + Qz + Cal + Tr = Di +$   
 472  $F(CO6.6)$ . As in the previous cases, a divariant field (dark grey shading) towards higher  
 473 temperatures is defined by pseudounivariant reactions with increasing  $X_{CO_2}$  in the fluid  
 474 composition (reaching up to 0.58). The described Di-Cal-Qz divariant field (dark grey;  
 475 Fig. 9D) partially overlaps with that of the tremolite-in conditions (light grey). At 300  
 476 MPa, the minimum temperature of this divariant field exactly fits that of the first Spl-in  
 477 reaction (430 °C). Taking into account that the sample with the product assemblage of  
 478 this reaction (09A-11; Table 1) is located only about 200 m away from the first

479 appearance of diopside, it could be suggested that Di-in temperatures must be somewhat  
480 higher than those of Spl-in (Fig. 9D).

481 Concerning *forsterite* stability, first P-T constraints are defined by equilibrium  $\text{Cal} + \text{Tr}$   
482  $+ \text{Fo} = \text{F} + \text{Dol} + \text{Di}$ , with a strongly changing Clapeyron slope and increasing  $X_{\text{CO}_2}$   
483 composition of fluid with decreasing pressure (number labels of pseudoinvariant points  
484 along the curve; Fig. 9D). This curve constrains the stability of the assemblage  
485  $\text{Cal} + \text{Tr} + \text{Fo}$ , observed in most rocks close to the contact with the peridotites (Table 1), to  
486 maximum values of  $P=500$  MPa (at  $300$  °C) and  $T=575$  °C (at  $200$  MPa). Within this  
487 field, the minimum temperature is further constrained by the reaction  $\text{F}(\text{H}_2\text{O}) + \text{Tr} +$   
488  $\text{Dol} = \text{F}(\text{CO6.6}) + \text{Cal} + \text{Fo}$  and its related divariant field with coexisting Tr, Dol, Cal  
489 and Fo and variable fluid composition (thin, grey, dashed pseudounivariant curves; Fig.  
490 9C). At  $300$  MPa this field ranges from  $510$  to  $560$  °C and partially overlaps with the  
491 field of minimum temperatures for Di-in (Fig. 9D). This is consistent with the mineral  
492 assemblage observed in rocks (sample 09A-1; Table 1) sampled close to the contact  
493 with the peridotites. Additional information can be obtained from both chlorite and  
494 clinohumite. The former has been observed at least in one Fo and Spl-bearing sample  
495 (09A-4; Table 1). Both reactions  $\text{Clc} + \text{Chu} = \text{H}_2\text{O} + \text{Fo} + \text{Spl}$  and  $\text{F}(\text{H}_2\text{O}) + \text{Dol} + \text{Clc}$   
496  $= \text{F}(\text{CO6.6}) + \text{Cal} + \text{Spl} + \text{Fo}$  are chlorite-breakdown reactions producing coexisting Fo  
497 and Spl, consistent with the observed rock assemblages (Table 1, Fig. 8G), and  
498 indicating minimum temperature conditions ranging from  $525$  to  $600$  °C at  $300$  MPa  
499 (Fig. 9D). Equilibria indicating the observed coexistence of clinohumite and olivine  
500 (Table 1, Fig. 8G) are the already mentioned  $\text{Clc} + \text{Chu} = \text{H}_2\text{O} + \text{Fo} + \text{Spl}$ , and also  $\text{H}_2\text{O}$   
501  $+ \text{Dol} + \text{Fo} = \text{Cal} + \text{Chu} + \text{F}(\text{CO6.6})$ . The stability of clinohumite increases towards  
502 higher temperatures with increasing fluorine contents (Rice, 1980). Taking this into  
503 account and attending to petrogenetic grids in Fig. 9 (A to C), it could be suggested that  
504 clinohumite-bearing assemblages sampled close to the contact with the peridotites  
505 might have reached maximum temperatures above  $700$  °C.

506 In conclusion, phase relations modelling in the KCMASHC system suggest the  
507 following approximate temperature ranges for the observed metamorphic zones of the  
508 Nieves Unit contact aureole at the maximum, geologically consistent, pressure of  $300$   
509 MPa (Fig. 9D): forsterite ( $> 510$  °C; probably around  $700$  °C), diopside ( $510$ – $430$  °C),  
510 tremolite ( $430$ – $360$  °C), phlogopite ( $360$ – $330$  °C).

511

512 *Microstructural Analysis*

513

514 Calcite (dolomite poor) marbles occur as strongly deformed rocks, displaying a variety  
515 of conspicuous microstructures in calcite grains (Fig. 8A, F): elongated grains defining  
516 a main foliation, curved twins, undulose extinction or mortar textures. The presence of  
517 subgrains and new recrystallized grains is common. Irregular (lobate) grain boundaries  
518 are also observed, pointing to the occurrence of grain boundary migration  
519 recrystallization. Dolomite-bearing marbles, on the contrary, commonly show a  
520 granoblastic texture (Fig. 8B).

521 Besides a general – though irregular – trend of calcite grain size increase from lower to  
522 higher metamorphic grades (Table 2), a variation of marble microstructures with  
523 distance from the peridotites (and hence temperature) is observed. The more distant  
524 calcite marbles (phlogopite and tremolite zones) tend to preserve deformation features,  
525 such as S-C-C' structures, recording top-to-NW shearing (Fig. 8J) that are not observed  
526 in the strongly recrystallized high-T marbles from the diopside and forsterite zones. A  
527 secondary foliation, oblique with respect to the main composite ( $S_0$ - $S_1$ ) foliation and  
528 produced by grain boundary alignment of recrystallized grains, is observed in samples  
529 from the tremolite through the forsterite zones (Fig. 8K, H). All of these samples show  
530 evidences of dynamic recrystallization resulting from a combination of both subgrain  
531 rotation and grain boundary migration. However, marbles from the forsterite zone also  
532 show straight grain boundaries and calcite triple junctions that are indicative of variable  
533 degrees of static recrystallization (Fig. 8H, I). The latter process appears to have led in  
534 some cases to a partially annealed microstructure characterized by generally equant,  
535 polygonal calcite grains (Fig. 8I). However, in one of the forsterite zone samples (09A-  
536 1), finer-grained zones of recrystallized grains cut across the annealed, coarse-grained  
537 microstructural domains.

538 For samples from the diopside through the tremolite to the phlogopite zones (09A-7 to  
539 09A-20), plots of all orientation data are very similar to the plots of 1 point per grain.  
540 This similarity reflects the equigranular nature of these samples. In contrast, orientation  
541 data from 09A-1 and 09A-3 (forsterite zone) show a significant difference between plots  
542 of all of the collected EBSD data (not shown) and 1 point per grain data because of the  
543 heterogeneous grain size and of the grain size bias associated with the larger grains. For  
544 forsterite zone samples we therefore only considered the one point per grain data.

545 EBSD data from the different metamorphic zones of the carbonate footwall show a  
546 number of similarities. In most cases (Fig. 10), the pole figures record a crystallographic



547 preferred orientation (CPO) with alignment of the calcite  $c$ -axis with the pole to the main  
548  $S_0$ - $S_1$  foliation ( $Z$ ). This is most strongly pronounced in samples 09A-7 and 09A-20. In  
549 09A-1 the single  $c$ -axis cluster lies oblique to  $Z$  and is rotated in the direction of the  
550 macroscopically established top-to-NW sense of shear. In other samples a subordinate  
551 component of the  $c$ -axis orientation also lies oblique to the  $Z$  direction, again synthetic  
552 with respect to the direction of the macroscopically established top-to-NW sense of  
553 shear (Fig. 10). The angular relationships between the different concentrations on the  $c$ -  
554 axis pole figure (usually  $< 40^\circ$ ) are not consistent with these clusters being associated  
555 with twinning in the samples. Comparison with high strain calcite deformation  
556 experiments indicates that such a pattern in  $c$ -axis orientations is consistent with high  
557 shear strains (Barnhoorn *et al.*, 2004) with varying degrees of recrystallization (Pieri *et*  
558 *al.*, 2001a). Only in 09A-19, there is a less defined and more symmetric distribution of  
559  $c$ -axes (Fig. 10). This sample retains evidence for non-coaxial deformation in the form  
560 of well-developed S-C fabrics with C-planes dominated by fibrous tremolite (Fig. 8J)  
561 but again there is no significant asymmetry within the (0001) pole figure data. Along  
562 with all other samples no variation in  $+<a>$  and  $-<a>$  was observed (Fig. 10). This  
563 contrasts observation on non-coaxially deformed calcite marble where asymmetry in  
564  $+<a>$  and  $-<a>$  are recorded during both low- and high-T non-coaxial flow (Bestmann,  
565 2000; Pieri *et al.*, 2001b) and may reflect a strong component of high-temperature  
566 recrystallization and steady-state flow (Pieri *et al.*, 2001a), and/or a component of static  
567 recrystallization (Barnhoorn *et al.*, 2005) that is consistent with the microstructure  
568 observed in high-T marbles. The data presented here indicate that orthorhombic  
569 symmetry of fabrics with respect to the principal ( $S_0$ - $S_1$ ) foliation plane cannot be used  
570 to provide unambiguous constraints on the coaxial or non-coaxial nature of the  
571 deformation at high temperature and high-strain rate conditions. However, where  
572 asymmetry in the  $c$ -axis distribution relative to the foliation is recorded, then this  
573 appears to be synthetic with respect to the rotational component of the non-coaxial strain  
574 inferred from S-C fabrics and mesoscopic kinematic criteria.

575 Misorientation axes for calcite marble data record differences between samples. In  
576 samples where significant low-angle boundaries are preserved (09A-1, 09A-7, and 09A-  
577 20) there is a dominant misorientation axis concentration associated with the ' $a$ '  $<11$ -  
578  $20>$  direction. This direction is still common in 09A-3 and 09A-19 which also have a  
579 significant number of measurements ( $n > 1000$ ), but other orientations are also apparent  
580 associated with ' $f$ '  $<02$ - $21>$ , ' $m$ '  $<10$ - $10>$ . In samples where low-angle boundaries are

581 rare (09A-12 and 09A-18), misorientation axes are concentrated close to the  $\langle 0001 \rangle$   
582 direction. The observed variation in the misorientation axes reflects the operation of  
583 different slip systems in calcite with  $\langle 11\bar{2}0 \rangle$  corresponding to the common high  
584 temperature ( $> 400\text{ }^\circ\text{C}$ ) slip systems  $r\{10\bar{1}4\}\langle\bar{2}021\rangle$  and  $f\{10\bar{1}2\}\langle 10\bar{1}1 \rangle$ , whilst  
585 ‘m’ $\langle 10\bar{1}0 \rangle$  is consistent with deformation by  $\{0001\}\langle\bar{1}2\bar{1}0\rangle$  slip (De Bresser &  
586 Spiers, 1997). In some of the samples (09A-1, 09A-18, 09A-19), misorientation axis  
587 evidence for the operation of  $f\{10\bar{1}2\}\langle 0\bar{2}21 \rangle$  is consistent with low temperature  
588 deformation (De Bresser & Spiers, 1997) and this may reflect a lower temperature  
589 overprint that may also have been responsible for the localized zones of reduced grain  
590 size observed in the highest temperature sample (09A-1). Such a lower temperature  
591 overprint could have led to a finer grain size of samples 09A-18 and 09A-19 (Table 2) as  
592 a result of dynamic recrystallization dominated by subgrain rotation.

593 EBSD analysis has also been performed on a dolomite marble sample (09A-15) from the  
594 tremolite zone (Fig. 10). The CPO in this sample, although clearly marked by the  $c$ -axis  
595 distribution, is weaker than that generally recorded by calcite marbles and also shows  
596 different misorientation axes from most of the calcite-dominated samples. This contrast  
597 suggests the operation of a different set of slip systems, albeit including the common  
598  $(0001)\langle 2\bar{1}10 \rangle$  slip system (Wenk, 1985). The asymmetry of the  $c$ -axis distribution  
599 with respect to the  $S_0$ - $S_1$  foliation plane is synthetic with the rotational component of  
600 simple shear.

601

## 602 **Discussion**

603

604 The Nieves Unit is characterized by significant changes in styles and intensity of  
605 deformation, with strongly heterogeneous structural development being closely linked  
606 to an inverse metamorphic gradient that is controlled by distance from the hanging-wall  
607 Ronda peridotites. This variation is expressed by different deformation features at  
608 different structural position within the main regional syncline involving the studied unit.

609 This major structure may be interpreted as a result of footwall deformation within the  
610 general framework of bulk non-coaxial strain associated with top-to-the-NW shearing.

611 The normal limb and core region of the regional syncline are characterized by the  
612 occurrence of NE-SW trending, meso-scale parasitic folds, whereas in the metamorphic  
613 aureole of the inverted limb, isoclinal, intrafolial folds occur. The hinge lines of these  
614 latter folds tend to lie close to the stretching direction and are interpreted to have been

615 strongly rotated towards this direction during progressive deformation. The occurrence  
616 of a well-developed foliation and associated mineral lineation, together with isoclinal  
617 intrafolial folds in the marbles, indicates that these rocks record a significant amount of  
618 finite strain, although shear-sense indicators are rarely observed in the field. These  
619 features are consistent with progressive strain localisation in the inverted limb of the  
620 major syncline. As a matter of fact, the overturned fold limb of the regional syncline  
621 appears to constitute a SE dipping, thermally softened carbonate rock panel that  
622 underwent intense deformation and metamorphism associated with the emplacement of  
623 the Ronda peridotites.

624 Both field and thin section evidence indicate a limited syn-kinematic growth of silicate  
625 minerals (locally testified by the preferred orientation of early generations of tremolite  
626 and phlogopite, Fig. 8B, C). However, most silicate grain growth appears to have  
627 occurred statically, following the development of the composite planar fabric ( $S_0$ - $S_1$ ) and  
628 mainly post-dating the main internal deformation in the marbles (Fig. 8F). This suggests  
629 that high-T footwall deformation associated with peridotite emplacement occurred at a  
630 much faster rate with respect to heat diffusion, which continued well after peridotite  
631 emplacement. Estimated maximum temperatures in the metamorphic aureole range from  
632 values in excess of 510 °C (probably around 700 °C) close to the contact with the  
633 peridotites to < 350° C in the more distant, less thermally overprinted rocks, for the  
634 inferred maximum pressure of 300 MPa. Higher-pressure values are rather unlikely due  
635 to the complete lack of regional metamorphism of the Nieves Unit away from the  
636 aureole at the contact with the peridotites. Had the overlying tectonic units been  
637 significantly thicker than *c.* 10 km, the whole footwall (Nieves Unit) would have  
638 undergone greenschist facies metamorphism (which is not observed). Therefore, it can  
639 be realistically considered that the present-day geometry (taking erosion into account;  
640 see geological sections in Figs. 2 and 4) is representative of the original (Miocene)  
641 tectonic load on top of the Nieves Unit (Mazzoli and Martín-Algarra, 2011, their fig. 6).  
642 This is consistent with syn-orogenic extension (Argles *et al.*, 1999) of the Jubrique  
643 crustal rocks originally overlying the Ronda peridotites. The crustal succession was  
644 being tectonically attenuated as the Ronda peridotites were exhuming, so that the Los  
645 Reales Unit was already significantly thinned (essentially to its present-day thickness)  
646 when final emplacement on top of the Nieves Unit occurred (Mazzoli and Martín-  
647 Algarra, 2011, their fig. 6). A maximum temperature of *c.* 700 °C is consistent with a  
648 peridotite emplacement postdating the latest metamorphic event recorded within the

649 ultramafic body, which occurred at conditions of  $P = 1$  GPa and  $T = 800\text{--}900$  °C  
650 (obtained for the aluminous mafic rocks alternating with peridotites and sampled near  
651 the marbles section studied in this work; Morishita *et al.*, 2001). Such high P-T  
652 conditions are interpreted as corresponding to a sustained synkinematic decompression  
653 event (Garrido *et al.*, 2011) that took place well before the final peridotite emplacement  
654 described here. The general – though irregular – trend of increasing calcite grain size  
655 with metamorphic grade observed in the studied footwall carbonates confirms the  
656 fundamental control exerted by temperature on calcite recrystallization processes,  
657 although the variable amount of secondary phases (Table 2) present in our impure  
658 marbles is likely to have played a major role, resulting in complex calcite grain growth  
659 patterns (Ebert *et al.* 2007a, b). As a matter of fact, the irregular distribution of calcite  
660 grain size shown in Table 2 is likely to result from a complex interplay of different  
661 factors including original grain size, amount of impurities, differential stress and thermal  
662 regime controlling the dominant deformation mechanisms. The microstructure of calcite  
663 marbles, characterized by the occurrence of undulose extinction, subgrains and new  
664 recrystallized grains, is indicative of deformation by slip and climb of dislocations  
665 (dislocation creep). The analysed calcite marbles show a well-developed CPO at all  
666 metamorphic grades, for a wide range of grain sizes and different – though generally  
667 moderate – amounts of secondary phases (Table 2). This is consistent with the  
668 dominance of dislocation creep at all temperatures characterizing the studied  
669 metamorphic aureole. Both microstructures and CPOs show no indications for a switch  
670 in deformation mechanisms from dislocation to diffusion creep or to grain-size sensitive  
671 mechanisms even at the highest temperature conditions (forsterite zone). Such an  
672 interpretation is in general agreement with the experimental findings of Barnhoorn *et al.*  
673 (2004). The associated occurrence of grain boundary migration recrystallization  
674 (testified by the common presence of lobate grain boundaries) is also consistent with  
675 large strains and relatively high temperatures in calcite marbles (e.g. Barnhoorn *et al.*,  
676 2004). The generally symmetric CPO patterns suggest high-T plastic deformation,  
677 dynamic recrystallization and steady-state flow, probably followed by variable degrees  
678 of static recrystallization that may have weakened the CPO (Barnhoorn *et al.*, 2005). In  
679 the highest-grade forsterite zone, the presence of a carbonate melt may have also  
680 contributed to a weakening of the CPO. In fact, the highest temperatures close to the  
681 peridotite contact were potentially higher than the eutectic of marbles (e.g. Boettcher &  
682 Wyllie, 1969). Therefore, at least part of the microfabric suggesting static

683 recrystallization associated with thermal diffusion – and the related weakened CPO –  
684 could actually have resulted from grain growth following partial melting. Melt fractions  
685 – no matter how small – may additionally have controlled deformation processes in the  
686 highest-grade marbles by enhancing grain boundary sliding and migration, as well as  
687 rotation.

688 The lack of strong asymmetries in  $\langle a \rangle$  and  $-\langle a \rangle$  distribution in marbles from all  
689 metamorphic zones, suggesting the occurrence of a coaxial strain component (Bestmann,  
690 2000; Pieri *et al.*, 2001b), is consistent with bulk deformation by general shear and/or  
691 partitioning of the deformation into zones dominated by either non-coaxial or coaxial  
692 strain. Furthermore, the occurrence of minor zones of strain localization and grain size  
693 reduction (associated with subgrain rotation recrystallization) overprinting previously  
694 annealed calcite textures (e.g. sample 09A-1) suggests a complex interplay between  
695 thermal effects and deformation events. Notwithstanding this, a final static overprint  
696 appears to be dominant in carbonates throughout the metamorphic aureole. This is  
697 consistent with the interpretation that most of the petrologic features characterizing the  
698 metamorphosed rock panel (inverted limb of the Nieves Unit regional syncline) located  
699 immediately in the footwall to the Ronda peridotites were acquired following the  
700 emplacement of the mantle extrusion wedge. Continued heat transfer from the  
701 peridotites to the footwall succession led to post-kinematic silicate growth and locally –  
702 especially in the highest-T forsterite zone – to partial annealing of calcite marble  
703 textures. Following substantial cooling (Esteban *et al.*, 2004), horizontal crustal  
704 shortening was resumed – as testified by meso-scale refolding affecting both  
705 metamorphic and non-metamorphic parts of the Nieves Unit – probably in relation with  
706 NW-ward thrusting of the ‘Frontal Units’ of the Internal Domain over the Flysch and  
707 External Domains (Figs. 2 to 4). Such a late, SE-NW oriented shortening of the Nieves  
708 Unit occurred at much lower temperatures, as testified by the lack of metamorphic  
709 mineral assemblages along the axial plane foliation ( $S_2$ ) associated with the second-  
710 phase, NE-SW trending mesoscopic folds.

711

## 712 **Conclusions**

713

714 Structural analysis of the dominantly carbonate Nieves Unit located in the footwall to  
715 the Ronda mantle extrusion wedge unravelled strongly heterogeneous deformation  
716 accompanying a dramatic metamorphic gradient. Marbles within a several hundreds of

717 meters-thick metamorphic aureole record high strain in the form of a well-developed  
718 foliation and associated mineral lineation, accompanied by widespread isoclinal  
719 intrafolial folds. Field evidence for non-coaxial strain, although clearly consistent with  
720 top-to-the-NW shearing, appears to be subordinate. On the other hand, the  
721 microstructures of calcite marbles – particularly the lower-T phlogopite-tremolite ones –  
722 effectively record top-to-the-NW kinematics, whereas their CPOs suggest the possible  
723 occurrence of a coaxial strain component and therefore of an overall deformation by  
724 general shear. Where asymmetry in the *c*-axis distribution is observed with respect to  
725 the main composite foliation (sub-parallel to the shear plane, due to very likely high-  
726 strain values), this appears to be synthetic with respect to the rotational component of  
727 the non-coaxial strain inferred from mesoscopic kinematic criteria, this being consistent  
728 with large shear strains and high-T conditions. Our results indicate that large strains and  
729 attenuation of a thermally softened carbonate rock panel, probably under a general shear  
730 deformation regime, dominantly controlled structural development and marble textural  
731 fabrics in the metamorphic aureole in the footwall to the Ronda peridotites.  
732 Petrological characteristics and mineral assemblages within the zoned metamorphic  
733 aureole appear to have mostly developed after the final emplacement of the Ronda  
734 mantle extrusion wedge. Post-kinematic, continued heat transfer from the hanging-wall  
735 peridotites led to static growth of silicate assemblages and local partial annealing of  
736 calcite marble textures, especially in the highest-T zone in the immediate footwall.  
737 Following substantial cooling, renewed crustal shortening affected the Nieves Unit,  
738 probably in relation with foreland-directed thrusting.

739

#### 740 **Acknowledgments**

741 The paper greatly benefited from thoughtful and constructive reviews by M. Smit and  
742 M. Orozco, as well as from the useful comments by Editor M. Cho. Financial support  
743 by: (i) the University of Naples Federico II to SM; (ii) Project CGL-2009-09249 (MCI),  
744 and Research Groups RNM-208 and RNM-3715 (JA) to AMA; and (iii) Project  
745 CGL2009-12518/BTE (MEC) and Research Group RNM-145 to VLSV is gratefully  
746 acknowledged. EBSD data were obtained using instrumentation funded by ARC LIEF,  
747 NCRIS and Curtin University. SMR acknowledges support from Curtin University and  
748 the Australian Research Council Centre of Excellence for Core to Crust Fluid Systems.  
749 This is contribution 227 from the ARC CoE for Core to Crust Fluid Systems and TIGeR  
750 publication no. 434.

751

752 **References**

753

- 754 ANDRIEUX, J., FONTBOTE, J.M., & MATTAUER, M. 1971. Sur un modèle explicatif de  
755 l'arc de Gibraltar. *Earth and Planetary Science Letters*, **12**, 191–198.
- 756 ARGLES, T.W., PLATT, J.P. & WATERS, D.J. 1999. Attenuation and excision of a crustal  
757 section during extensional exhumation: the Carratraca Massif, Betic Cordillera,  
758 southern Spain. *Journal of the Geological Society of London*, **156**, 149–162.
- 759 BADERTSCHER, N.P. & BURKHARD, M. 2000. Brittle-ductile deformation in the Glarus  
760 thrust Lochseiten (LK) calc-mylonite. *Terra Nova*, **12**, 281–288.
- 761 BADERTSCHER, N.P., BEAUDOIN, G., THERRIEN, R. & BURKHARD, M. 2002. Glarus  
762 overthrust; a major pathway for the escape of fluids out of the Alpine Orogen.  
763 *Geology*, **30**, 875–878.
- 764 BALANYÀ, J.C., AZAÑÓN, J.M., SÁNCHEZ-GÓMEZ, M. & GARCÍA-DUEÑAS, V. 1993.  
765 Pervasive ductile extension, isothermal decompression and thinning of the  
766 Jubrique unit in the Paleogene (Alpujárride Complex, western Betics, Spain).  
767 *Comptes Rendus de l'Académie des Sciences de Paris*, **316**, 1595–1601.
- 768 BALANYA, J.C., GARCIA-DUEÑAS, V., AZAÑON, J.M. & SANCHEZ-GOMEZ, M. 1997.  
769 Alternating contractional and extensional events in the Alpujárride nappes of the  
770 Alboran Domain (Betics, Gibraltar Arc). *Tectonics*, **16**, 226–238.
- 771 BARNHOORN, A., BYSTRICKY, M., BURLINI, L. & KUNZE, K. 2004. The role of  
772 recrystallisation on the deformation behaviour of calcite rocks: large strain  
773 torsion experiments on Carrara marble. *Journal of Structural Geology*, **26**, 885–  
774 903, doi:10.1016/j.jsg.2003.11.024.
- 775 BARNHOORN, A., BYSTRICKY, M., BURLINI, L. & KUNZE, K. 2005. Post-deformational  
776 annealing of calcite rocks. *Tectonophysics*, **403**, 167–191,  
777 doi:10.1016/j.tecto.2005.04.008.
- 778 BESTMANN, M., KUNZE, K. & MATTHEWS, A. 2000. Evolution of a calcite marble shear  
779 zone complex on Thassos Island, Greece; microstructural and textural fabrics  
780 and their kinematic significance. *Journal of Structural Geology*, **22**, 1789–1807.
- 781 BOETTCHER, A.L. & WYLLIE, P.J. 1969. The system CaO–SiO<sub>2</sub>–CO<sub>2</sub>–H<sub>2</sub>O: IIIA  
782 second critical end-point on the melting curve at 32.5 kbars and 515 °C.  
783 *Geochimica et Cosmochimica Acta*, **33**, 611–632.

- 784 BURKHARD, M. 1993. Calcite twins, their geometry, appearance and significance as  
785 stress-strain markers and indicators of tectonic regime; a review. *Journal of*  
786 *Structural Geology*, **15**, 351–368.
- 787 BUSCH, J.P. & VAN DER PLUIJM, B.A. 1995. Calcite textures, microstructures and  
788 rheological properties of marble mylonites in the Bancroft shear zone, Ontario,  
789 Canada. *Journal of Structural Geology*, **17**, 677–688.
- 790 CONNOLLY, J.A.D. 1990. Multivariable phase diagrams: an algorithm based on  
791 generalized thermodynamics (4 Mb). *American Journal of Science*, **290**, 666–  
792 718.
- 793 CONNOLLY, J.A.D. 2009. The geodynamic equation of state: what and how.  
794 *Geochemistry Geophysics Geosystems*, **10**, Q10014,  
795 doi:10.1029/2009GC002540.
- 796 CONNOLLY, J.A.D. & KERRICK, D.M. 1987. An algorithm and computer program for  
797 calculating composition phase diagrams. *CALPHAD*, **11**, 1–55.
- 798 CONNOLLY, J.A.D. & TROMMSDORFF, V. 1991. Petrogenetic grids for metacarbonate  
799 rocks – pressure-temperature phase-diagram projection for mixed-volatile  
800 systems. *Contributions to Mineralogy and Petrology*, **108**, 93–105.
- 801 CUEVAS, J., ESTEBAN, J.J. & TUBÍA, J.M. 2006. Tectonic implications of the granite dyke  
802 swarm in the Ronda peridotites (Betic Cordilleras, Southern Spain). *Journal of*  
803 *the Geological Society, London*, **163**, 631–640.
- 804 DE BRESSER, J.H.P. & SPIERS, C.J. 1997. Strength characteristics of the r, f, and c slip  
805 systems in calcite. *Tectonophysics*, **272**, 1–23.
- 806 DIDON, J., DURAND-DELGA M. & KORNPORST, J. 1973. Homologies géologiques entre  
807 les deux rives du Détroit de Gibraltar. *Bulletin de la Société géologique de*  
808 *France*, **15**, 77–105.
- 809 DÜRR, S.H. 1967. Geologie der Serrania de Ronda und ihrer südwestlichen Ausläufer  
810 (Andalusien). *Geologica Romana*, **6**, 1–73.
- 811 EBERT, A., HERWEGH, M., EVANS, B., PFIFFNER, A., AUSTIN, N. & VENNEMANN, T.  
812 2007a. Microfabrics in carbonate mylonites along a large-scale shear zone  
813 (Helvetic Alps). *Tectonophysics*, **444**, 1–26, doi:10.1016/j.tecto.2007.07.004.
- 814 EBERT, A., HERWEGH, M. & PFIFFNER, A. 2007b. Cooling induced strain localization in  
815 carbonate mylonites within a large-scale shear zone (Glarus thrust, Switzerland).  
816 *Journal of Structural Geology*, **29**, 1164–1184, doi:10.1016/j.jsg.2007.03.007.



- 817 ESTEBAN, J.J., CUEVAS, J., TUBÍA, J.M., GIL-IBARGUCHI, J.I. & SEWARD, D. 2005.  
818 Metamorfismo, exhumación y termocronología de la unidad de Yunquera  
819 (Alpujarrides occidentales, Cordilleras Béticas). *Revista de la Sociedad*  
820 *Geológica de España*, **18**, 61–74.
- 821 ESTEBAN, J.J., SÁNCHEZ-RODRÍGUEZ, L., SEWARD, D., CUEVAS, J. & TUBÍA, J.M. 2004.  
822 The late thermal history of the Ronda area. *Tectonophysics*, **389**, 81–92.
- 823 ESTEBAN, J.J., CUEVAS, J., TUBÍA, J.M., LIATI, A., SEWARD, D. & GEBAUER, D. 2007.  
824 Timing and origin of zircon-bearing chlorite schists in the Ronda peridotites  
825 (Betic Cordilleras, Southern Spain). *Lithos*, **99**, 121–135.
- 826 ESTEBAN, J.J., CUEVAS, J., VEGAS, N. & TUBÍA J.M. 2008. Deformation and kinematics  
827 in a melt-bearing shear zone from the Western Betic Cordilleras (Southern  
828 Spain). *Journal of Structural Geology*, **30**, 380–393.
- 829 ESTEBAN, J.J., TUBÍA, J.M., CUEVAS, J., VEGAS, N., SERGEEV, S. & LARIONOV, A. 2011.  
830 Peri-Gondwanan provenance of pre-Triassic metamorphic sequences in the  
831 western Alpujarride nappes (Betic Cordillera, southern Spain). *Gondwana*  
832 *Research*, **20**, 443–449, doi:10.1016/j.gr.2010.11.006
- 833 GARRIDO, C.J., GUEYDAN, F., BOOTH-REA, G., PRECIGOUT, J., HIDAS, K., PADRÓN-  
834 NAVARTA, J.A. & MARCHESI, C. 2011. Garnet lherzolite and garnet-spinel  
835 mylonite in the Ronda peridotite: Vestiges of Oligocene backarc mantle  
836 lithospheric extension in the western Mediterranean. *Geology*, **39**, 927–930,  
837 doi:10.1130/G31760.1.
- 838 HEITZMANN, P. 1987. Calcite mylonites in the Central Alpine “root zone”.  
839 *Tectonophysics*, **135**, 207–215.
- 840 HOEPPENER, R., HOPPE, H., MOLLAT, H., MUCHOW, S. DÜRR, S.H. & KOCKEL, F. 1963.  
841 Über den westlichen abschnitt der Betischen Kordilleren und seine beziehungen  
842 zum gesamtrogen. *Geologische Rundschau*, **53**, 269–296.
- 843 HOEPPENER, R., HOPPE, H., DÜRR, S.H. & MOLLAT, H. 1964. Ein querschnitt durch die  
844 Betischen Kordilleren bei Ronda (SW Spanien). *Geologie en Mijnbouw*, **43**,  
845 282–298.
- 846 HOLLAND, T. J. B. & POWELL, R. 1998. An internally consistent thermodynamic data set  
847 for phases of petrologic interest. *Journal of Metamorphic Geology*, **16**, 309–343.
- 848 IANNACE, A., BONARDI, G., D’ERRICO, M., MAZZOLI, S., PERRONE, V. & VITALE, S.  
849 2005. Structural setting and tectonic evolution of the Apennine Units of northern  
850 Calabria. *Comptes Rendus-Geoscience*, **337**, 1541–1550.

- 851 IANNACE, A., VITALE, S., D'ERRICO, M., *ET AL.* 2007. The Lungro–Verbicaro Unit  
852 (northern Calabria, Italy): A record of Tethyan paleomargin evolution and  
853 Miocene convergence, continental subduction, and exhumation of HP–LT rocks.  
854 *Journal of the Geological Society, London*, **164**, 1165–1186, doi:10.1144/0016-  
855 76492007-017.
- 856 LUNDEEN, M.T. 1978. Emplacement of the Ronda peridotite, Sierra Bermeja, Spain.  
857 *Geological Society of America Bulletin*, **89**, 172–180.
- 858 MARTÍN-ALGARRA, A. 1987. *Evolución geológica alpina del contacto entre las Zonas*  
859 *Internas y las Zonas Externas de la Cordillera Bética*. [Ph. D. Thesis] University  
860 of Granada, 1171 p.
- 861 MARTÍN-ALGARRA, A. 2004 (coord.). Unidades Frontales de las Zonas Internas. *In*:  
862 Vera, J.A. (ed.) *Geología de España*, Sociedad Geológica de España - Instituto  
863 Geológico y Minero de España, Madrid, 396–401.
- 864 MARTÍN-ALGARRA, A. & ESTEVEZ A. 1984. La brèche de la Nava: dépôt continental  
865 synchrone de la structuration pendant le Miocène inférieur des Zones Internes de  
866 l'ouest des Cordillères Bétiques. *Comptes Rendus de l'Académie de Sciences de*  
867 *Paris*, **299**, 463–466.
- 868 MARTIN-ALGARRA, A., MAZZOLI, S., PERRONE, V. & RODRIGUEZ-CAÑERO, R. 2009.  
869 Variscan tectonics in the Malaguide Complex (Betic Cordillera, Southern Spain):  
870 stratigraphic and structural Alpine vs. pre-Alpine constraints from the Ardales  
871 area (Province of Malaga). II: Structure. *Journal of Geology*, **117**, 263–284.
- 872 MARTÍN-ALGARRA, A., O'DOHERTY, L., AGUADO, R. & GURSKY, H.J. 1998.  
873 Estratigrafía, petrografía y significado paleogeográfico de las radiolaritas  
874 jurásicas de tipo austroalpino de la unidad de las Nieves (Formación Parauta,  
875 Rondaides, Cordillera Bética Occidental). *Geogaceta*, **24**, 211–214.
- 876 MARTÍN-ALGARRA, A. & VERA, J.A. 2004. Evolución de la Cordillera Bética. *In*: VERA,  
877 J.A. (ed.) *Geología de España*, Sociedad Geológica de España - Instituto  
878 Geológico y Minero de España, Madrid, 437–444.
- 879 MAZZOLI, S. & MARTÍN-ALGARRA, A. 2011. Deformation partitioning during  
880 transpressional emplacement of a 'mantle extrusion wedge': the Ronda  
881 peridotites, western Betic Cordillera, Spain. *Journal of the Geological Society*,  
882 **168**, 373–382, doi:10.1144/0016-76492010-126.

- 883 MORISHITA, T., ARAI, S. & GERVILLA, F. 2001. High-pressure aluminous mafic rocks  
884 from the Ronda peridotite massif, southern Spain: significance of sapphirine-  
885 and corundum-bearing mineral assemblages. *Lithos*, **57**, 143–161.
- 886 OBATA, M. 1980. The Ronda peridotite: garnet-, spinel-, and plagioclase lherzolite  
887 facies and the P-T trajectories of a high temperature mantle intrusion. *Journal of*  
888 *Petrology*, **21**, 533–572.
- 889 O'DOHERTY, L., MARTÍN-ALGARRA, A., GURSKY, H.J. & AGUADO, R. 2001. The  
890 Middle Jurassic radiolarites and pelagic limestones of the Nieves Unit (Rondaide  
891 Complex, Betic Cordillera): Basin starvation in a rifted marginal slope of the  
892 western Tethys. *International Journal of Earth Sciences (Geol. Rundsch.)*, **90**,  
893 831–846.
- 894 OROZCO, M. & ALONSO-CHAVES, F.M. 2012. Kilometre-scale sheath folds in the  
895 western Betics (south of Spain). *International Journal of Earth Sciences (Geol*  
896 *Rundsch)*, **101**, 505–519.
- 897 PFIFFNER, O. A. 1982. Deformation mechanisms and flow regimes in limestones from  
898 the Helvetic Zone of the Swiss Alps. *Journal of Structural Geology*, **4**, 429–442.
- 899 PIERI, M., BURLINI, L., KUNZE, K., OLGAARD, D.L. & STRETTON, I.C. 2001a.  
900 Rheological and microstructural evolution of Carrara marble with high shear  
901 strain: results from high temperature torsion experiments. *Journal of Structural*  
902 *Geology*, **23**, 1393–1413.
- 903 PIERI, M., KUNZE, K., BURLINI, L., STRETTON, I.C., OLGAARD, D.L., BURG, J.-P. &  
904 WENK, H.R. 2001b. Texture development of calcite by deformation and dynamic  
905 recrystallisation at 1000 K during torsion experiments of marble to large strains.  
906 *Tectonophysics*, **330**, 119–140.
- 907 PLATT, J. P., ARGLES, T. W., CARTER, A., *ET AL.* 2003. Exhumation of the Ronda  
908 peridotite and its crustal envelope: constraints from thermal modelling of a P-T-  
909 time array. *Journal of the Geological Society*, **160**, 655–676.
- 910 RENNER, J., EVANS, B. & SIDDIQI, G. 2002. Dislocation creep of calcite. *Journal of*  
911 *Geophysical Research*, **107** (B12), 2364, doi:10.1029/2001JB001680.
- 912 RICE, J.M. 1977. Progressive metamorphism of impure dolomitic limestone in the  
913 Marysville Aureole, Montana. *American Journal of Science*, **277**, 1–24.
- 914 RICE, J.M. 1980. Phase equilibria involving humite minerals in impure dolomitic  
915 limestones. Part I. Calculated stability of clinohumite. *Contributions to*  
916 *Mineralogy and Petrology*, **71**, 219–235.

- 917 RUTTER, E.H., CASEY, M. & BURLINI, L. 1994. Preferred crystallographic orientation  
918 development during the plastic and superplastic flow of calcite rocks. *Journal of*  
919 *Structural Geology*, **16**, 1431–1446.
- 920 SÁNCHEZ-NAVAS, A., DE OLIVEIRA-BARBOSA, R.D.C., GARCÍA-CASCO, A. & MARTÍN-  
921 ALGARRA, A. 2012. Transformation of andalusite to kyanite in the Alpujarride  
922 Complex (Betic Cordillera, S Spain): Geologic implications. *Journal of*  
923 *Geology*, **120**, 557–574. doi:10.1086/666944.
- 924 SÁNCHEZ RODRÍGUEZ L. & GEBAUER, D. 2000. Mesozoic formation of pyroxenites and  
925 gabbros in the Ronda area (southern Spain), followed by Early Miocene  
926 subduction metamorphism and emplacement into the middle crust: U-Pb  
927 sensitive high-resolution ion microprobe dating of zircon. *Tectonophysics*, **316**,  
928 19–44.
- 929 SCHMID, S.M., BOLAND, J.N. & PATERSON, M.S. 1977. Superplastic flow in finegrained  
930 limestone. *Tectonophysics*, **43**, 257–291.
- 931 SCHMID, S.M., PATERSON, M.S. & BOLAND, J.N. 1980. High temperature flow and  
932 dynamic recrystallisation in Carrarra marble. *Tectonophysics*, **65**, 245–280.
- 933 SCHMID, S.M., PANOZZO, R. & BAUER, S. 1987. Simple shear experiments on calcite  
934 rocks: rheology and microfabric. *Journal of Structural Geology*, **9**, 747–778.
- 935 TROMMSDORFF, V. & CONNOLLY, J.A.D. 1990. Constraints on phase diagram topology  
936 for the system: CaO-MgO-SiO<sub>2</sub>-H<sub>2</sub>O-CO<sub>2</sub>. *Contributions to Mineralogy and*  
937 *Petrology*, **104**, 1–7.
- 938 TUBÍA, J.M. 1994. The Ronda peridotites (Los Reales nappe): an example of the  
939 relationship between lithospheric thickening by oblique tectonics and late  
940 extensional deformation within the Betic Cordillera (Spain). *Tectonophysics*,  
941 **238**, 381–398.
- 942 TUBÍA, J. M. & CUEVAS, J. 1986. High-temperature emplacement of the Los Reales  
943 peridotite nappe (Betic Cordillera, Spain). *Journal of Structural Geology*, **8**,  
944 473–482.
- 945 TUBÍA, J.M., CUEVAS, J. & GIL IBARGUCHI, J.I. 1997. Sequential development of the  
946 metamorphic aureole beneath the Ronda peridotites and its bearing on the  
947 tectonic evolution of the Betic Cordillera. *Tectonophysics*, **279**, 227–252.
- 948 TUBÍA, J. M. & GIL IBARGUCHI, I. 1991. Eclogites of the Ojén nappe: a record of  
949 subduction in the Alpujarride Complex (Betic Cordilleras, southern Spain).  
950 *Journal of the Geological Society, London*, **148**, 801–804.

- 951 ULRICH, S., SCHULMANN, K. & CASEY, M. 2002. Microstructural evolution and  
952 rheological behaviour of marbles deformed at different crustal levels. *Journal of*  
953 *Structural Geology*, **24**, 979–995.
- 954 VAN DER WAL, D. & VISSERS, R.L.M. 1996. Structural petrology of the Ronda peridotite,  
955 SW Spain: deformation history. *Journal of Petrology*, **37**, 23–43.
- 956 VAN WEES, J.D., DE JONG, K. & CLOETING, S. 1992. Two-dimensional P-T-t modelling  
957 and the dynamics of extension and inversion in the Betic Zone (SE Spain).  
958 *Tectonophysics*, **203**, 305–324.
- 959 VITALE, S. & MAZZOLI, S. 2005. Influence of object concentration on finite strain and  
960 effective viscosity contrast: insights from naturally deformed packstones.  
961 *Journal of Structural Geology*, **27**, 2135–2149.
- 962 VITALE, S. & MAZZOLI, S. 2009. Finite strain analysis of a natural ductile shear zone in  
963 limestones: insights into 3-D coaxial vs. non-coaxial deformation partitioning.  
964 *Journal of Structural Geology*, **31**, 104–113, doi:10.1016/j.jsg.2008.10.011.
- 965 VITALE, S., WHITE, J.C., IANNACE, A. & MAZZOLI, S. 2007. Ductile strain partitioning in  
966 micritic limestones, Calabria, Italy: the roles and mechanisms of intracrystalline  
967 and intercrystalline deformation. *Canadian Journal of Earth Sciences*, **44**, 1587–  
968 1602.
- 969 WENK, H.R. 1985. Carbonates. In: Preferred Orientation in Deformed Metals and Rocks.  
970 An Introduction to Modern Texture Analysis, Academic Press, pp. 361–384.
- 971 WHITNEY, D.L. & EVANS B.W., 2010. Abbreviations for names of rock-forming  
972 minerals. *American Mineralogist*, **95**, 185–187.
- 973

974 **Figure Captions**

975

976 **Fig. 1.** Tectonic sketch map of the Betic Cordillera, showing the Ronda peridotites  
977 outcrop area (boxed SW-most sector).

978

979 **Fig. 2.** Tectonic sketch map of the western Betic Cordillera and regional geological  
980 cross-section X-X' (after Mazzoli and Martín-Algarra, 2011, modified). Box shows  
981 location of area mapped in detail (Fig. 3).

982

983 **Fig. 3.** Geological map of field study area (showing sample location) and trace of cross-  
984 section reproduced in Fig. 4.

985

986 **Fig. 4.** Geological cross-section (roughly parallel to the Ronda-San Pedro de Alcantara  
987 road) through the leading edge of the Ronda peridotites at Sierra Bermeja (after Mazzoli  
988 and Martín-Algarra, 2011, modified), showing projected location of the studied samples.  
989 Zoning of the metamorphic aureole (shaded) in the Nieves Unit is shown by means of  
990 the following index minerals: talc (tc), phlogopite (phl), tremolite (tr), diopside (di), and  
991 forsterite (fo). Key for stratigraphic units: (1) Norian dolostones and (1') dolomite  
992 marbles; (2) Rhaetian marls and (2') calcschists; (3) Rhaetian limestones and (3') calcite  
993 marbles; (4) Lower Jurassic cherty limestones and marls and (4') marbles including  
994 quartz lenses and calcschists; (5) Middle Jurassic-Paleogene (mainly marly) condensed  
995 succession and (5') calc-schists; (6) Nava Breccia Fm.

996

997 **Fig. 5.** Field examples of structural features in the Nieves Unit in the footwall to the  
998 Ronda peridotites. (A) View of the tectonic contact with the overlying Ronda peridotites  
999 (Cerro Corona area). (B) View of the hinge zone of the regional syncline, including  
1000 second-order overturned folds (Fuenfría area). (C) Composite planar fabric ( $S_0$ - $S_1$ ) in  
1001 dolomite marble (km 19.5 of the A-473 road from Ronda to San Pedro de Alcantara). (D)  
1002 Close-up of the boxed area in (C), showing minor folds in the hinge zone of a larger  
1003 syncline. (E) Composite planar fabric ( $S_0$ - $S_1$ ; horizontal) in metamorphosed Jurassic  
1004 cherty limestones (Torrecilla area). Note symmetric pressure shadows around framboidal  
1005 pyrite grains (arrowed). (F) Composite planar fabric ( $S_0$ - $S_1$ ) displaced and overgrown by  
1006 phlogopite-tremolite clot in metamorphosed Norian levels (dolomite marbles of the  
1007 Cerro Alcojona area).

1008

1009 **Fig. 6.** Outcrop examples of structural features in the Nieves Unit. (A) Mineral lineation  
1010 ( $L_1$ ) defined by elongated tremolite (arrowed) and dolomite crystals lying on the main  
1011 foliation in metamorphosed Norian levels (dolomite marbles at km 19.5 of the A-473  
1012 road from Ronda to San Pedro de Alcantara). (B) Early intrafolial folds in dolomite  
1013 marbles (Cerro Alcojona area). (C) Late (post-metamorphic) folds affecting the main  
1014 composite planar fabric ( $S_0$ - $S_1$ ) in dolomite marbles (km 19.5 of the A-473 road from  
1015 Ronda to San Pedro de Alcantara). (D) Asymmetric ( $z$ -shaped looking towards SW)  
1016 parasitic folds affecting bedding ( $S_0$ ) in the normal limb of the regional syncline  
1017 (Jurassic cherty limestones of the Torrecilla area). (E) Late kink bands affecting the  
1018 main composite planar fabric ( $S_0$ - $S_1$ ) along the San Pedro de Alcantara road.

1019

1020 **Fig. 7.** Orientation data (lower hemisphere, equal-area projections) for structures in the  
1021 Nieves Unit. (A) Poles to bedding ( $S_0$ )/composite planar fabric ( $S_0$ - $S_1$ ; metamorphic  
1022 aureole); pole to the best-fit great circle (or  $\pi$ -girdle, plunging  $19^\circ$  toward  $54^\circ$ N)  
1023 provides a statistical axis consistent with NE-SW trending folding. (B) Mineral lineation  
1024 ( $L_1$ ) in silicate-bearing marbles. (C) Hinges of isoclinal, intrafolial folds. (D) Poles to  
1025 axial surfaces of isoclinal, intrafolial folds. (E) Hinge lines of late, open to tight folds  
1026 within metamorphic aureole. (F) Poles to axial surfaces of late, open to tight folds within  
1027 metamorphic aureole.

1028

1029 **Fig. 8.** Thin section microphotographs (crossed polars) showing representative  
1030 petrological and microstructural features of the studied marble samples (mineral name  
1031 abbreviations after Whitney and Evans, 2010). (A) Intensely deformed, high-T calcite  
1032 marble (sample 09A-02; forsterite zone). (B) Granoblastic, mainly dolomite marble  
1033 (with scarce, “dusty” calcite grains) with a thin folded layer of phlogopite (sample 09A-  
1034 15; tremolite zone). (C) Palmed aggregate of amphibole subparallel to the main rock  
1035 foliation as indicated by the white dashed line (sample 09A-16; tremolite zone). (D)  
1036 Xenoblastic spinel grains associated with calcite and large phlogopite flakes (sample  
1037 09A-11; tremolite zone). (E) Typical mineral assemblage of clinopyroxene, calcite and  
1038 quartz-bearing rock (sample 09A-08; diopside zone). (F) Hypidioblastic clinopyroxene  
1039 and amphibole grains overgrowing strongly deformed calcite grains (sample 09A-01;  
1040 forsterite zone). (G) Typical high-grade mineral assemblage of olivine-clinohumite-  
1041 spinel marble close to the contact with peridotite (sample 09A-24; forsterite zone). (H)

1042 High-T calcite marble (sample 09A-3; forsterite zone) showing lobate grain boundaries  
1043 (red arrows), straight grain boundaries and triple junctions (yellow arrows) and  
1044 secondary foliation (sf) defined by recrystallized grains oblique to the main composite  
1045 foliation (horizontal; NW is to the right of the picture). (I) High-T marble with equant  
1046 calcite grains showing both lobate and straight boundaries (sample 09A-25; forsterite  
1047 zone). (J) Lower-T calcite marble (sample 09A-19; tremolite zone) displaying S-C-C'  
1048 fabrics (NW is to the right of the picture). (K) Lower-T calcite marble (sample 09A-20;  
1049 phlogopite zone) showing secondary foliation (sf) defined by recrystallized grains  
1050 oblique to the main composite foliation (horizontal; NW is to the right of the picture).

1051

1052 **Fig. 9.** Calculated P-T projections for the  $K_2O$ -CaO-MgO- $Al_2O_3$ - $SiO_2$ - $H_2O$ - $CO_2$  system  
1053 with the following minerals (abbreviations after Whitney and Evans, 2010): calcite  
1054 (Cal), clinocllore (Clc), clinohumite (Chu), diopside (Di), dolomite (Dol), forsterite  
1055 (Fo), microcline (Mc), phlogopite (Phl), quartz (Qz), spinel (Spl) and tremolite (Tr).  
1056 Abbreviation for the fluid solution is F. All curves in (A) correspond to univariant  
1057 equilibria. Field b-d in (A) is enlarged in diagrams (B), (C) and (D). Note that minimum  
1058 pressure in these cases widens towards 50 MPa. Thick and thin dashed curves  
1059 correspond to univariant and pseudounivariant equilibria, respectively (see text for  
1060 details). Big circles and small filled circles along univariant curves correspond to  
1061 invariant and pseudoinvariant points, respectively. Different grey areas represent  
1062 divariant fields in which pseudounivariant equilibria are stable with the same solid  
1063 phases and changing fluid composition ( $X_{CO_2}$  always increases with temperature). In  
1064 (D), thick dashed line at a constant pressure of 300 MPa acts as reference for obtaining  
1065 the temperature ranges for the relevant phases observed in the studied rocks (upper part  
1066 of the diagram).

1067

1068 **Fig. 10.** CPO data for calcite marble samples from: (i) forsterite zone (09A-1, 09A-3);  
1069 (ii) diopside zone (09A-7); (iii) tremolite zone (09A-18, 09A-19); and (iv) phlogopite  
1070 zone (09A-20). Dolomite marble sample (09A-15) is from the tremolite zone. All  
1071 projections are lower hemisphere and equal area. Contour lines are at intervals of 0.5  
1072 Multiples of Uniform Density (MUD) and the maximum MUD is given to two  
1073 significant figures. For forsterite zone samples, heterogeneous grain size gives rise to a  
1074 grain-size dependent bias in standard pole figures. For 09A-1 and 09A-3 data are  
1075 therefore shown as 1 point per grain. For other samples, pole figure data (columns 1-5)



1076 represents all of the collected EBSD data. For comparison, 1 point per grain data for all  
1077 samples is given in column 6, along with the MUD and the total number of analysed  
1078 grains. Misorientation axes data are calculated for minimum angular misorientations  
1079 between adjacent EBSD analyses of 2-10° and are given with MUD and number of  
1080 misorientation axes. Orientation of oblique foliation is indicated in column 1 for  
1081 samples (09A-3, 19, 20) whose microstructure is shown in Fig. 8.

**Table 1:** Mineral assemblages of the studied marbles. Names abbreviations after Whitney and Evans (2010)

Samp. Area*	Met. Zone**	Sample	Cal	Dol	Qz	Mc	Chl	Phl	Amp	Cpx	Scp	Ol	Chu	Spl	Sph	Mag		
CC	forsterite	09A-1	x		x			x	x	x								
CC		09A-2	x					x				x						
CC		09A-3	x						x			x					x	
CC		09A-4	x	x			x	x	x			x			x		x	
CA		09A-21	x	x				x	x			x	x	x			x	
CA		09A-22	x	x				x	x			x			x		x	
CA		09A-23	x	x				x	x								x	
CA		09A-24	x	x				x	x				x	x	x		x	
CA		09A-25	x					x	x								x	
CC		diopside	09A-5	x		x			x		x							x
CC	09A-6		x		x			x	x	x	x					x	x	
CC	09A-7		x		x			x									x	
CC	09A-8		x		x	x		x			x	x					x	x
CC	09A-9		x		x			x	x	x							x	x
CC	tremolite	09A-10	x	x				x									x	
CC		09A-11	x	x				x	x						x		x	
CC		09A-12	x	x	x			x	x								x	
CC		09A-13	x	x				x									x	
CC		09A-14	x	x				x									x	
CC		09A-15	x	x				x									x	
CC		09A-16	x	x			x	x	x								x	
CC		09A-17	x	x				x	x								x	
CC		09A-18	x	x				x	x								x	
CC		09A-19	x					x									x	
CC	phlogopite	09A-20	x		x			x									x	

\* Sampling area. CC: Cerro de los Cascajares; CA: Cerro Alcojona

\*\* Metamorphic zone, after Martín-Algarra (1987)

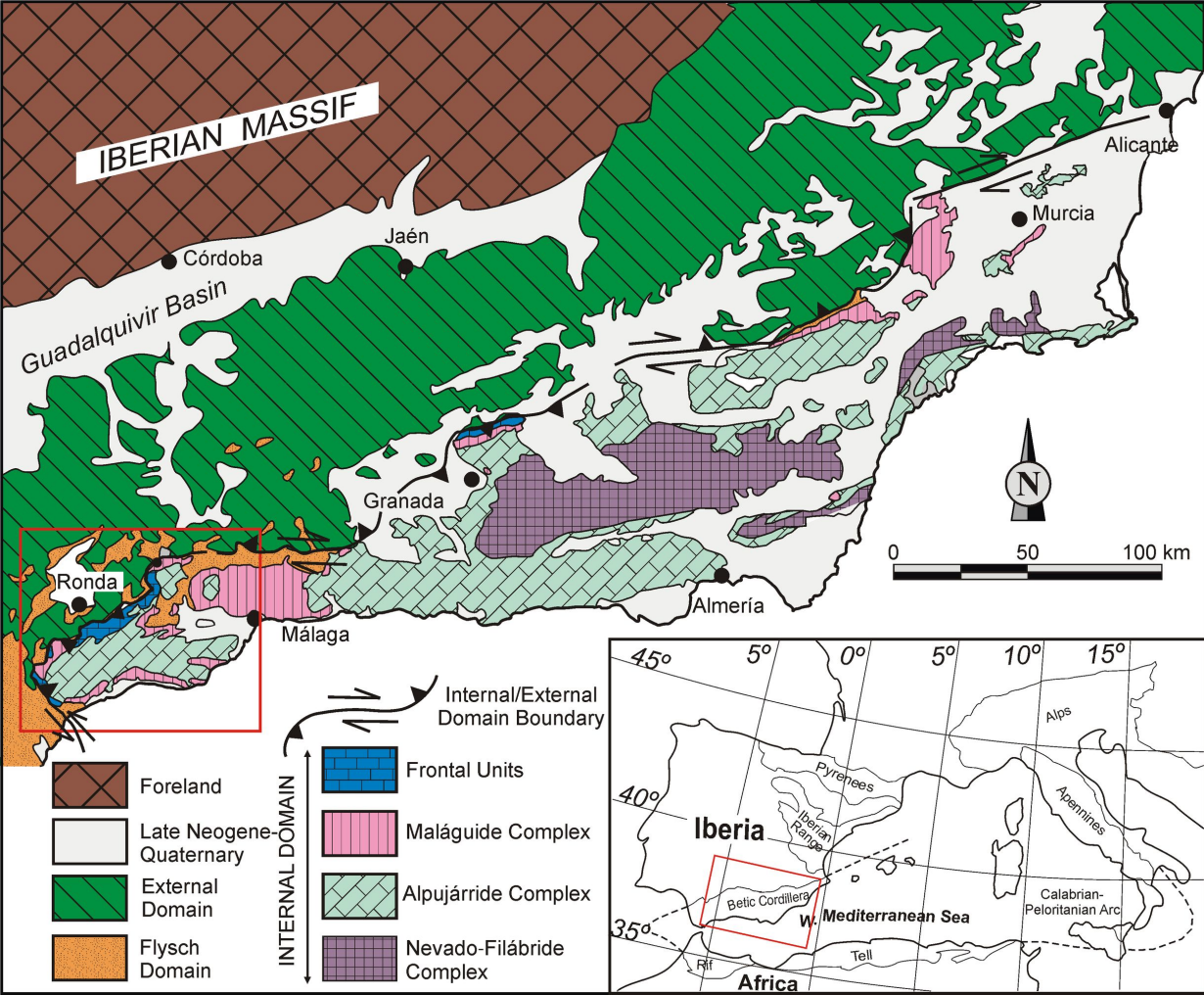
**Table 2:** Modal analysis and carbonate grain size analysis of the studied marbles.

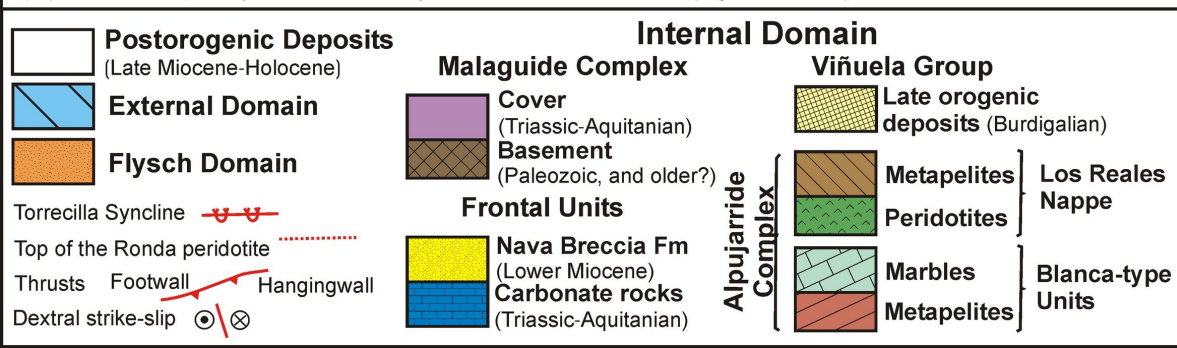
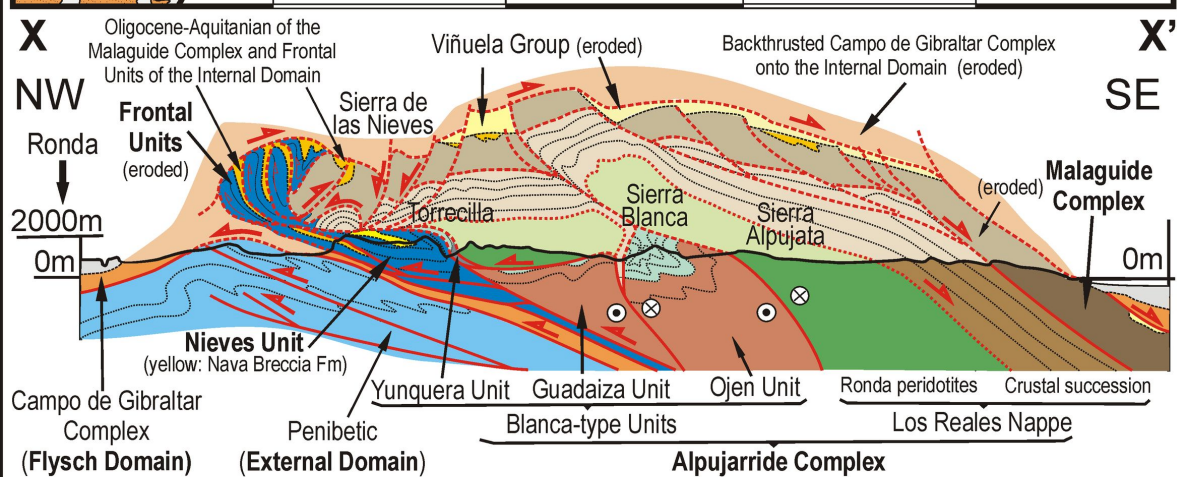
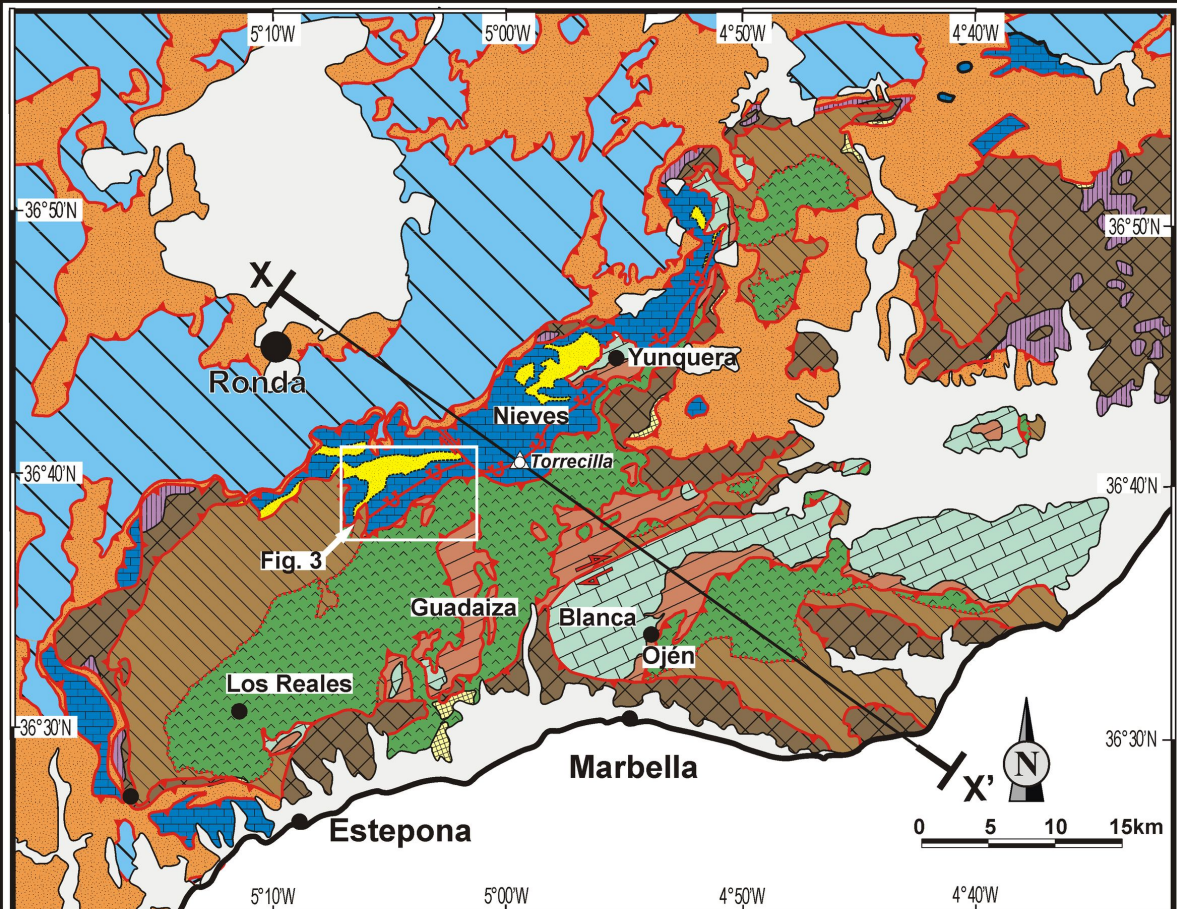
Sampling Area*	Metamorphic Zone**	Sample	Impurities	Dmin	Dmax	Dmedian
CC	forsterite	09A-1	6.5 n = 4700	9	1329	178 ( $\pm 153$ ) n = 713
CC		09A-3	6.8 n = 6000	68	2083	230 ( $\pm 136$ ) n = 512
CC	diopside	09A-7	12.0 n = 8000	35	429	111 ( $\pm 52$ ) n = 705
CC	tremolite	09A-12	10.1 n = 10000	51	1586	354 ( $\pm 244$ ) n = 561
CC		09A-15	7.2 n = 5000	55	666	143 ( $\pm 59$ ) n = 1218
CC		09A-18	17.8 n = 8000	22	394	70 ( $\pm 31$ ) n = 740
CC		09A-19	16.6 n = 10000	12	96	30 ( $\pm 12$ ) n = 619
CC	phlogopite	09A-20	11.0 n = 10000	26	437	112 ( $\pm 55$ ) n = 614

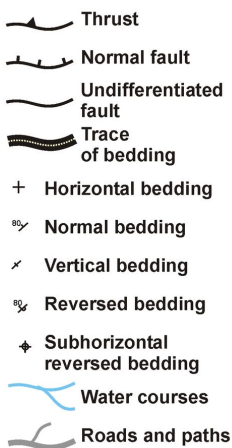
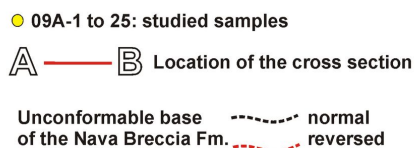
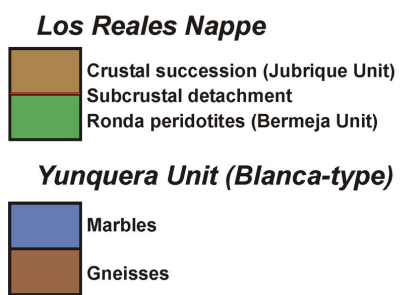
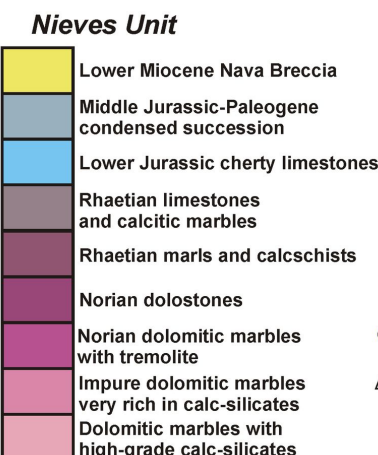
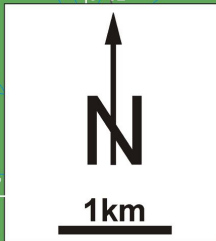
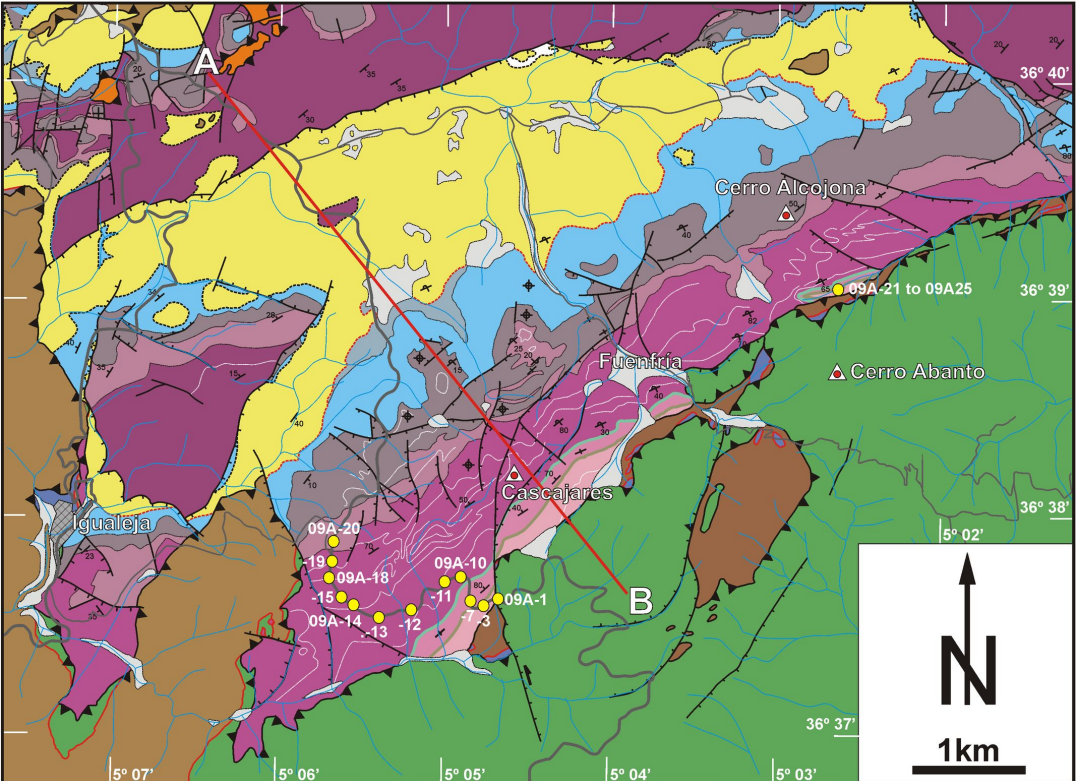
\* CC: Cerro de los Cascajares.

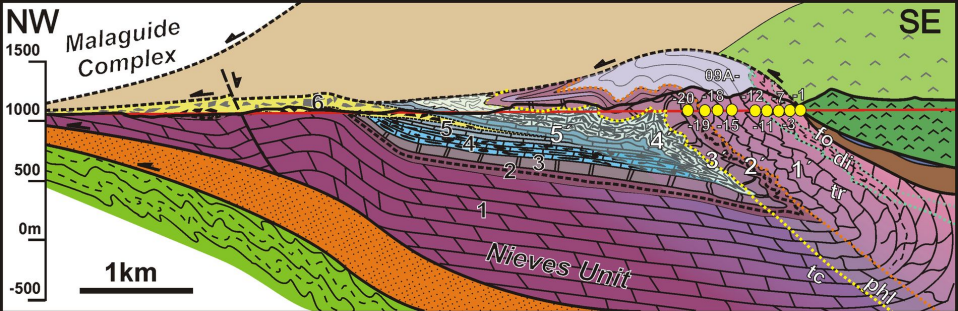
\*\* After Martín-Algarra (1987).

Impurities = abundance of the non-carbonate minerals (in vol. %; n = number of counted points); Dmin = minimum size (in  $\mu\text{m}$ ) of the carbonate minerals; Dmax = maximum size (in  $\mu\text{m}$ ) of the carbonate minerals; Dmedian = median size (in  $\mu\text{m}$ ) of the carbonate minerals (standard deviation values reported in brackets; n = number of measured grains).

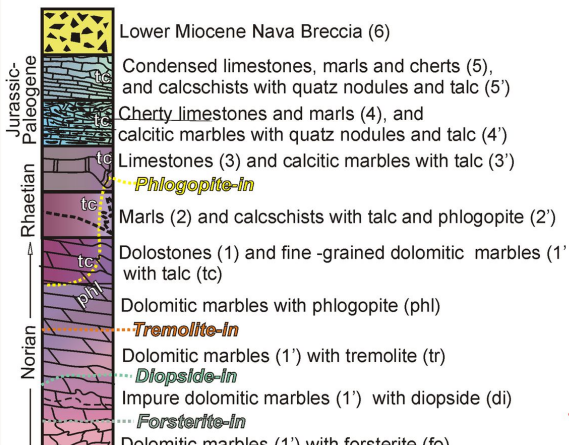




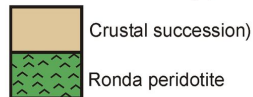




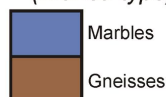
### Nieves Unit



### Los Reales Nappe



### Yunquera Unit (Blanca-type)



Campo de Gibraltar Complex

Penibetic

Road from Ronda to San Pedro de Alcántara, with location of the studied samples (projected)

